



HAL
open science

Micromodeling

Amna Rekik, Frédéric Lebon

► **To cite this version:**

Amna Rekik, Frédéric Lebon. Micromodeling. Numerical Modeling of Masonry and Historical Structures, pp.295-349, 2019, 10.1016/B978-0-08-102439-3.00009-9 . hal-02336722

HAL Id: hal-02336722

<https://hal.science/hal-02336722>

Submitted on 2 Sep 2020

HAL is a multi-disciplinary open access archive for the deposit and dissemination of scientific research documents, whether they are published or not. The documents may come from teaching and research institutions in France or abroad, or from public or private research centers.

L'archive ouverte pluridisciplinaire **HAL**, est destinée au dépôt et à la diffusion de documents scientifiques de niveau recherche, publiés ou non, émanant des établissements d'enseignement et de recherche français ou étrangers, des laboratoires publics ou privés.



Distributed under a Creative Commons Attribution 4.0 International License

Micromodeling

A. Rezik¹ and F. Lebon²

¹*INSA CVL, Univ. Orléans, Univ. Tours, Orléans, France,* ²*Aix-Marseille Univ. CNRS Centrale Marseille LMA, Marseille, France*

9.1 Introduction

Masonry is one of the oldest construction materials and is still commonly used today to build houses or structures because of its strength, solidity, durability, resistance, its elegant appearance, etc. However, masonry, which is not generally thought to be a highly technological material, shows highly complex behavior, due in particular, to the interactions between the components (mortar, bricks) and the anisotropy induced by the direction of the joints, which are a source of weakness. Masonry structures were classically designed on the basis of empirical rules. Modern virtual methods of design have been developed only quite recently. Structures built long ago were extremely stable because they were massive. In modern masonry buildings, the walls are very thick, requiring the stability to be studied from a theoretical point of view, especially when wind or earthquakes are a concern. The strength of the masonry is thus critical and it is necessary to study the solidity of the structure using fine models and numerical simulations as in the case of concrete and steel structures. Other problems such as cracks also require more detailed studies on the design of masonry structures.

Mortar joints are usually weaker than masonry units, which explains the existence of planes of weakness along which cracks can propagate. Several models have been developed and presented in the literature for studying and predicting the behavior of masonry structures. Depending on the level of accuracy and simplicity required, either macro- or micromodeling strategies can be used for this purpose.

In continuum structural and macromodels, bricks, mortar, and brick–mortar interfaces are smoothed out into a homogeneous continuum, the average properties of which are identified at the level of the constituents, taking their geometric arrangement into account. This approach is applicable when the dimensions of a structure are sufficiently large for the ratio between the

average stresses and average strains to be acceptable such as the macromodels (classical no-tension models; Di Pasquale, 1992; Lourenco, 1998; Marfia and Sacco, 2005) that have been widely developed in the past.

During the last few decades, other models have been developed such as micropolar Cosserat continuum models (Masiani and Trovalusci, 1996; Sulem and Muhlhaus, 1997) as well as applications of the mathematical theories of homogenization to periodic (Anthoine, 1995; Luciano and Sacco, 1997; Ushaksarei and Pietruszczak, 2002) and nonperiodic media (Alpa and Monetto, 1994). To describe the inelastic behavior of structural masonry, some authors have combined homogenization techniques with a continuum damage mechanics approach (Pegon and Anthoine, 1997; Zucchini and Lourenço, 2004; Chengqing and Hong, 2006). Other authors such as Alpa and Monetto (1994) and de Buhan and de Felice (1997) have defined suitably macroscopic yield failure surfaces. Macroapproaches obviously require a preliminary mechanical characterization of the model, based on experimental laboratory or in situ tests (Gabor et al., 2005, 2006).

In studies based on microanalysis, two main approaches have been used: the simplified approach and the detailed micromodeling approaches. Simplified methods consist of modeling the bricks, mortar, and interface separately by adopting suitable constitutive laws for each component. This approach gives highly accurate results, especially at a local level. A simplified micromodel is an intermediate approach, where the properties of the mortar and the mortar interface unit are lumped into a common element, while expanded elements are used to model the brick units. Although this model reduces the computational cost of the analysis, some accuracy is obviously lost.

Several authors (Lotfi and Shing, 1994; Lourenço and Rots, 1997; Pegon et al., 2001; Pelissou and Lebon, 2009) have established that the interface elements reflect the main interactions occurring between bricks and mortar. Several methods have been presented for modeling the behavior of interfaces with zero thickness and predicting their failure modes. Giambanco and Di Gati (1997), for example, expressed the constitutive law at the interface in terms of contact traction and the relative displacements of the two surfaces interacting at the joint. The fracture of the joint and the subsequent sliding are associated with the interface yield condition. A method based on limit analysis combined with a homogenization technique was recently shown to be a powerful structural analysis tool, giving accurate collapse predictions: de Buhan and de Felice (1997), for example, presented a homogenized model of this kind that can be used for the limit analysis of masonry walls. The units are assumed in this model to be infinitely resistant and the joints are taken to be interfaces with zero thickness having a friction failure surface. In addition, the brittle damage model developed in Luciano and Sacco (1997) and Pelissou and Lebon (2009)

involves an elementary cell composed of units, mortar, and a finite number of fractures at the interfaces.

This chapter summarizes recently developed models based on micromechanics (linear and nonlinear homogenization methods) and the coupling of this approach with structural analysis and/or brittle fracture theory and creep of masonry components to predict local and overall behavior of masonry and also to reproduce creep or prevent collapse of these structures.

9.2 Coupling between homogenization techniques and damage theory

9.2.1 Accounting for damaged brick–mortar interface

Interface models for assessing the safety of civil and historical masonry constructions have attracted considerable attention, since their resistance depends to a large extent on the brick–mortar interfacial properties. In fact, mortar joints are usually less strong than masonry units, which explains the existence of planes of weakness along which cracks can propagate. Several models have been developed and presented in the literature for studying and predicting the behavior of masonry structures. Depending on the level of accuracy and simplicity required, either macro- or micromodeling strategies can be used for this purpose.

This section aims to identify the crack-length evolution laws governing a recently proposed constitutive equation (Rekik and Lebon, 2010, 2012), generalized in Raffa et al. (2016, 2017) with a small number parameters for microcracked interfaces of masonry structures. It also aims to study the effect of the masonry structure size and the load type on these identified parameters. Experimental tests (Gabor et al., 2006; Fouchal et al., 2009) on small and large masonry panels have been used to estimate the small number of parameters describing the microcrack evolution law and leading to the best fit between the numerical and experimental tests. In the case of a masonry structure under a compression load, the evaluation of the local numerical fields requires us to add a unilateral contact condition to avoid the overlap between the bricks and the joints constituents. In our first approach and for the sake of simplicity, we do not introduce friction between the brick and mortar units.

9.2.1.1 Effective properties of the brick–mortar lamina

Due to the fact that damage occurs mostly at the interface between brick and mortar materials, we assume the existence of an extremely thin layer of material between each brick unit and its mortar joint. The mechanical properties of this layer are obtained by applying an asymptotic limit analysis procedure (Raffa et al., 2017). For this purpose, it is proposed first to obtain the mechanical properties of the 3D material obtained by homogenizing those of

brick and mortar. Assuming brick and mortar to be isotropic and linear elastic materials, the homogenization of the brick–mortar lamina can be carried out exactly using an analytical homogenization formulation, as described in Rekik and Lebon (2010, 2012). The homogeneous equivalent undamaged material, denoted hereafter by HEM^u , is transversally isotropic and characterized by the effective compliance tensor \tilde{S}^u written in the form of Eq. (9.1) with respect to the classical Voigt notation. In what follows, exponents h and v correspond to bed and head joints, respectively; and e_3 and e_1 represent the HEM_h^u and HEM_v^u revolution axis, respectively, as shown in Fig. 9.1.

$$\tilde{S}^{uh} = \begin{pmatrix} \frac{1}{\tilde{E}_1^0} & -\frac{\tilde{\nu}_{12}^0}{\tilde{E}_1^0} & -\frac{\tilde{\nu}_{13}^0}{\tilde{E}_1^0} & & & \\ -\frac{\tilde{\nu}_{12}^0}{\tilde{E}_1^0} & \frac{1}{\tilde{E}_1^0} & -\frac{\tilde{\nu}_{13}^0}{\tilde{E}_1^0} & & & \\ -\frac{\tilde{\nu}_{13}^0}{\tilde{E}_1^0} & -\frac{\tilde{\nu}_{13}^0}{\tilde{E}_1^0} & \frac{1}{\tilde{E}_3^0} & & & \\ & & & \frac{1}{\tilde{G}_{23}^0} & & \\ & & & & \frac{1}{\tilde{G}_{23}^0} & \\ & & & & & \frac{1}{\tilde{G}_{12}^0} \end{pmatrix} \quad (9.1)$$

For further details about the method of obtaining the components of \tilde{S}_u^h see Rekik and Lebon (2010).

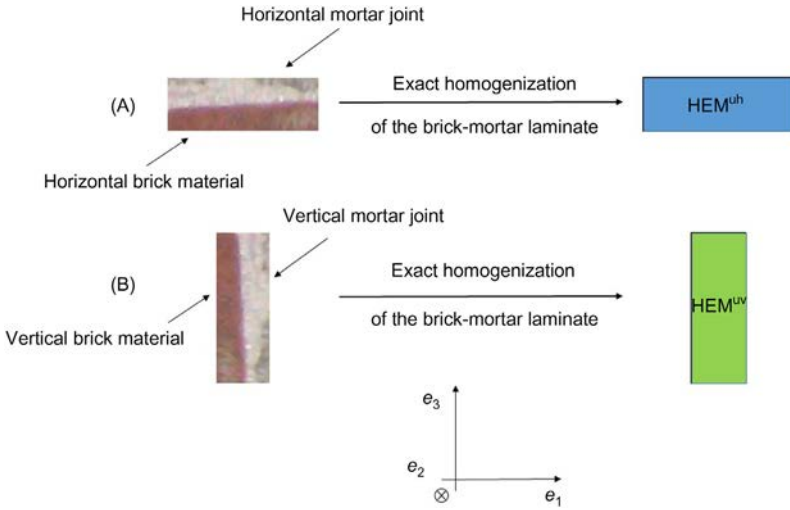


FIGURE 9.1 Determination of the elastic properties of the third material (a brick/mortar lamina) located at bed (A) and head (B) joints.

9.2.1.2 Effective properties of the microcracked material HEM^c

In the previous step, in the case of bed joints, an uncracked homogeneous material HEM_h^u was defined, based on the known properties of brick and mortar. Now assuming the presence of parallel microcracks to the e_1 axis in this material, it is necessary to determine its effective properties. Many studies have dealt with assessing the effective elastic properties of damaged materials with defects of various kinds (holes and/or cracks). The choice of modeling method depends here mainly on the interactions between cracks.

For the sake of simplicity, we started to model the degradation of the brick–mortar interface taking only the interactions between microcracks and neglecting the interactions with the matrix of the HEM^u material.

Moreover, we assume the existence of a small number of rectilinear cracks $2l^{(k)}$ in length. To solve this 2D problem it is proposed to apply the method proposed by Tsukrov and Kachanov (2000) to determine the equivalent properties of the damaged HEM^u material. The accuracy of this model, which generally depends on the density of the cracks, is satisfactory up to quite small distances between cracks (distances much smaller than the crack width). Rectilinear cracks are assumed to be located on the plane (e_1, e_3) in a representative area $A = L_0e$, where L_0 is the bed mortar length and e is the thickness of the microcracked HEM^u material.

In the case of the present 2D problem, the Kachanov model includes a global parameter called the crack density, which is defined by the number and the length of all the cracks given by:

$$\rho = \frac{1}{A} \sum_k (l^{(k)})^2 \quad (9.2)$$

The main result obtained with the Kachanov model is that the average value of the crack opening displacement (COD) vector “ b ” is colinear with the average stress $\bar{\sigma}$ as follows:

$$\langle b \rangle = n \cdot \bar{\sigma} \cdot B \quad (9.3)$$

where n is a vector normal to the crack. The components of the symmetric B second-order tensor depend on those of the uncracked homogeneous HEM^u material, that is, on the components of \hat{S}_u^h and on the orientation of the crack with respect to the matrix anisotropy:

$$\begin{cases} B_{tt} = C(1 - D \cos(2\phi)) \\ B_{nn} = C(1 + D \cos(2\phi)) \\ B_{nt} = CD(\sin(2\phi)) \end{cases} \quad (9.4)$$

where l is the length of the half-representative rectilinear microcrack in the HEM^u material, as shown in Fig. 9.2.

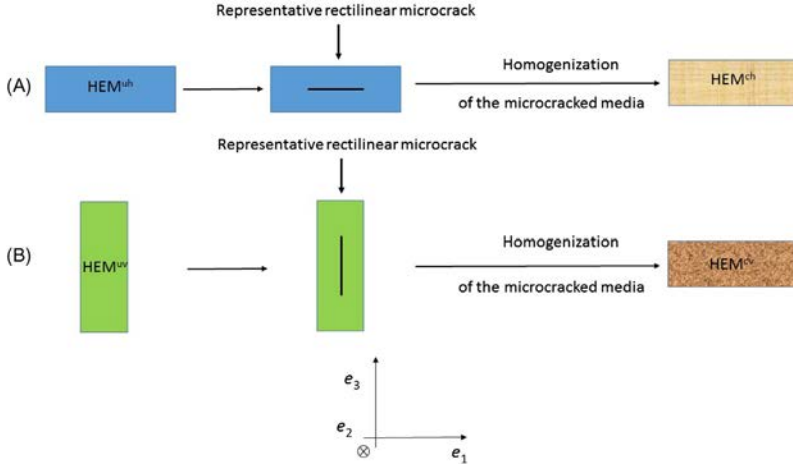


FIGURE 9.2 Assessment of the effective properties of the microcracked bed (A) and head (B) joints using the Kachanov model.

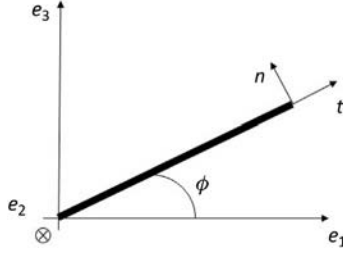


FIGURE 9.3 Local crack vectors and the principal axis of the masonry.

We recall that ϕ is the angle between the vector t tangential to the crack and the principal axis e_1 , as illustrated in Fig. 9.3. C and D are scalars that are independent of the representative microcrack half-length parameter l , and are given by:

$$\left\{ \begin{array}{l} C = \frac{\pi \sqrt{\tilde{E}_1^{uh}} + \sqrt{\tilde{E}_3^{uh}}}{4 \sqrt{\tilde{E}_1^{uh} \tilde{E}_3^{uh}}} \left(\frac{1}{\tilde{G}_{13}^{uh}} - 2 \frac{\tilde{\nu}_{13}^{uh}}{\tilde{E}_1^{uh}} + \frac{2}{\sqrt{\tilde{E}_1^{uh} \tilde{E}_3^{uh}}} \right)^{\frac{1}{2}} \\ D = \frac{\sqrt{\tilde{E}_1^{uh}} + \sqrt{\tilde{E}_3^{uh}}}{\sqrt{\tilde{E}_1^{uh}} + \sqrt{\tilde{E}_3^{uh}}} \end{array} \right. \quad (9.5)$$

where \tilde{E}_1^{uh} , \tilde{E}_3^{uh} , $\tilde{\nu}_{13}^{uh}$, \tilde{G}_{13}^{uh} are the elastic engineering constants of the crack-free HEM_h^{uh} material. On the principal axes, the effective engineering moduli

of HEM_c denoting the homogeneous material equivalent to the damaged HEM^u are given by:

$$\left\{ \begin{array}{l} \frac{\tilde{E}_1^c}{\tilde{E}_1^u} = \frac{1}{1 + 2\rho \sin^2 \phi (B_{tt} \cos^2 \phi + B_{mm} \sin^2 \phi - B_{nt} \sin(2\phi)) \tilde{E}_1^u} \\ \frac{\tilde{E}_3^c}{\tilde{E}_3^u} = \frac{1}{1 + 2\rho \cos^2 \phi (B_{tt} \sin^2 \phi + B_{mm} \cos^2 \phi + B_{nt} \sin(2\phi)) \tilde{E}_3^u} \\ \frac{\tilde{G}_{13}^c}{\tilde{G}_{13}^u} = \frac{1}{1 + \rho (B_{mm} \sin^2(2\phi) + B_{tt} \cos^2(2\phi) - B_{nt} \sin(4\phi)) \tilde{G}_{13}^u} \\ \frac{\tilde{\nu}_{13}^c}{\tilde{E}_1^c} = \frac{\tilde{\nu}_{13}^u}{\tilde{E}_1^u} \end{array} \right. \quad (9.6)$$

In the bed masonry joints, the cracks are assumed to run parallel to the principal axis e_1 , that is, with the crack orientation $\phi = 0$. Under plane stress conditions, the components of the compliance tensor \tilde{S}^c in the (e_1, e_3) plane read:

$$\tilde{S}^{ch} = \tilde{S}^c(0) = \begin{pmatrix} \frac{1}{\tilde{E}_1^{uh}} & -\frac{\tilde{\nu}_{13}^{uh}}{\tilde{E}_1^{uh}} & 0 \\ -\frac{\tilde{\nu}_{13}^{uh}}{\tilde{E}_1^{uh}} & \left(\frac{1}{\tilde{E}_3^{uh}} + 2\rho B_{mm}(0) \right) & 0 \\ 0 & 0 & \left(\frac{1}{G_{13}^{uh}} + \rho B_{tt}(0) \right) \end{pmatrix} \quad (9.7)$$

where

$$\begin{cases} B_{tt}(0) = C(1 - D) \\ B_{mm}(0) = C(1 + D) \\ B_{nt}(0) = 0 \end{cases} \quad (9.8)$$

As shown in relations (9.7), the effective properties of the cracked lamina are sensitive to the effective properties of the uncracked lamina \tilde{S}_u^h and to the representative crack length. Inverting the compliance tensor \tilde{S}^{ch} gives the corresponding stiffness tensor \tilde{C}^{ch} associated with the properties of HEM^{ch} .

9.2.1.3 Interface constitutive law

It has been assumed that cracks exist only in the plane (e_1, e_3) parallel to either the principal axis e_1 (in the case of bed joints) or to the e_3 vector (in the case of head joints). We have therefore focused only on the pair of

components $(\tilde{C}_{3333}^{ch}, \tilde{C}_{3131}^{ch})$ and $(\tilde{C}_{1111}^{cv}, \tilde{C}_{1313}^{cv})$ corresponding to the bed and head interface stiffness, respectively. Now focusing on the head interface stiffnesses, the inversion of the compliance tensor \tilde{S}^{ch} leads to expressing the components $(\tilde{C}_{3333}^{ch}, \tilde{C}_{3131}^{ch})$ as a function of the microcrack density parameter ρ and the angle ϕ is null:

$$\tilde{C}_{3333}^{ch} = \frac{\alpha_{33}^h + \rho\beta_{33}^h}{\alpha_{33}^{0h} + \rho\beta_{33}^{0h} + \rho^2\gamma_{33}^{0h}} \quad \text{and} \quad \tilde{C}_{1313}^{ch} = \frac{1}{2} \frac{\alpha_{13}^h + \rho\beta_{13}^h}{\alpha_{13}^{0h} + \rho\beta_{13}^{0h} + \rho^2\gamma_{13}^{0h}} \quad (9.9)$$

where $\alpha_{ij}^h, \beta_{ij}^h, \alpha_{ij}^{0h}, \beta_{ij}^{0h}$ are scalars that are independent of the crack density parameter ρ . The normal and tangential stiffness of the bed interfaces are determined as follows:

$$C_N^h = \frac{\tilde{C}_{3333}^{ch}}{e}(\text{eyields}0) \quad \text{and} \quad C_T^h = \frac{\tilde{C}_{3131}^{ch}}{e}(\text{eyields}0) \quad (9.10)$$

Replacing ρ by the term l^2/eL_0^h in expressions (9.9), we obtain:

$$C_N^h = \frac{\beta_{33}^h L_0^h}{\gamma_{33}^{0h} l^2} = \frac{L_0^h}{2B_{mn}(0)l^2} \quad \text{and} \quad C_T^h = \frac{\beta_{13}^h L_0^h}{\gamma_{13}^{0h} l^2} = \frac{L_0^h}{4B_{tt}(0)l^2} \quad (9.11)$$

As the components B_{mn} and B_{tt} depend on the half crack length l (see relation (9.2)), the expressions for the interface stiffness C_N and C_T at the bed position read:

$$C_N^h = \frac{L_0^h}{2C(1+D)l^2} \quad \text{and} \quad C_T^h = \frac{L_0^h}{4C(1-D)l^2} \quad \text{where } dl \geq 0 \quad (9.12)$$

dl is the increment of crack length, assumed to be positive during the shear loading. It is worth noting that the properties of the material HEM^{cv} , which is transversally isotropic with $e1$ as the revolution axis, are deduced from those of the material HEM^{ch} by making a simple 90 degree rotation. Therefore, the normal and tangential stiffness of the head joints read:

$$C_N^v = \frac{\tilde{C}_{1111}^{cv}}{e}(\text{eyields}0) = \frac{L_0^v}{L_0^h} C_N^h \quad \text{and} \quad C_T^v = \frac{\tilde{C}_{1313}^{cv}}{e}(\text{eyields}0) = \frac{L_0^v}{L_0^h} C_T^h \quad (9.13)$$

where L_0^h is the bed mortar joint length. These defined stiffnesses can be clearly seen to decrease as the crack length increases with respect to the applied load F (or shear stress τ). In addition, they are closely related to the law of microcrack evolution $l = f(F \text{ or } \tau)$, which will be identified in the case of masonry structures of various sizes under loads of various kinds in the following section. The crack-length evolution is assumed to show a similar tendency at the head and bed interfaces.

9.2.1.4 Estimation of the representative law of microcrack evolution based on experimental tests

In view of Eq. (9.10), one of the most important steps consists of defining, testing, and validating a law governing the crack-length evolution. An alternative simpler solution consists of defining directly by choosing crack lengths at several points on experimental diagrams. Hereafter, it is necessary to distinguish between the case of quasibrittle failures, with which the “stress–strain” diagram shows a “plateau” in the postpeak load part (in the case of nonconfined masonry) and those showing a softening and sliding parts after the peak in the load. In fact, numerical tests carried out on nonconfined (Rekik and Lebon, 2010) and confined masonry panels have shown that the laws of crack-length evolution available so far in the case of nonconfined masonry are not able to reproduce the softening and sliding parts seen in the case of the confined masonries.

Hereafter, for numerical computations, the geometry and boundary conditions are given in Fig. 9.4 (with the confining pressure σ) for the case of seven bricks. Table 9.1 lists the mechanical properties of the bricks and mortar constituting the prism (Gabor et al., 2006). Because of the symmetry of the prism problem, only half-structures will be used in the computations. In what follows, bricks and mortar joints will be modeled using Q4 quadrangular finite elements.

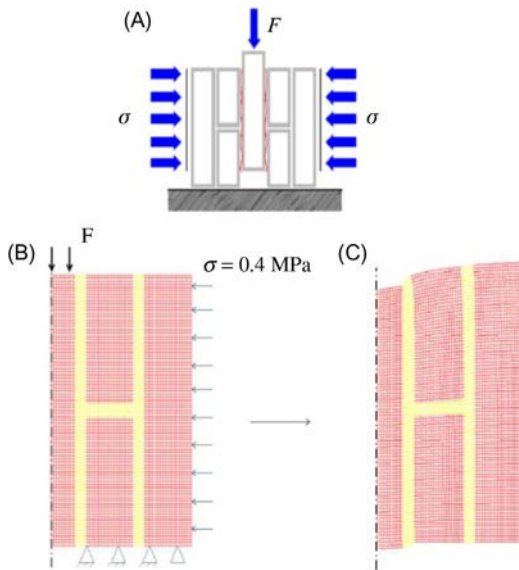


FIGURE 9.4 Initial geometrical configuration and loading conditions imposed on a small confined wall (A and B); deformation of the small wall in a shear test (C).

TABLE 9.1 Mechanical properties of the prism and wall masonry constituents.

Young's modulus (MPa) of full brick	12,800
Poisson's ratio of full brick	0.2
Young's modulus (MPa) of mortar	4000
Poisson's ratio of mortar	0.2

Source: From Gabor, A., Ferrier, E., Jacquelin, E., Hamelin, P., 2005. Analysis of the inplane shear behavior of FRP reinforced hollow brick masonry walls. *Struct. Eng. Mech.* 19, 237–260; Gabor, A., Bennani, A., Jacquelin, E., Lebon, F., 2006. Modelling approaches of the in-plane shear behaviour of unreinforced and FRP strengthened masonry panels. *Comput. Struct.*, 74, 277–288.

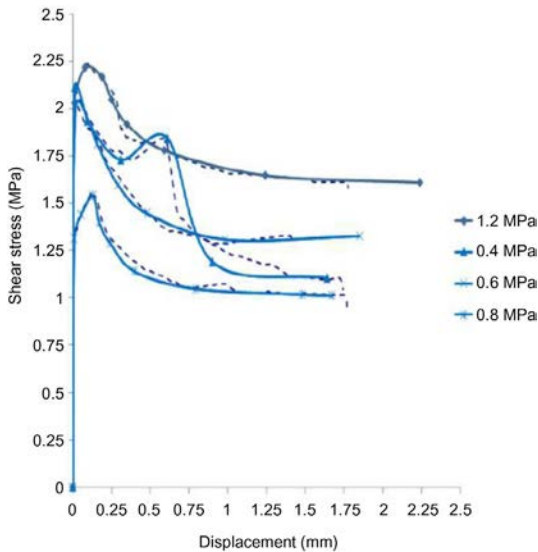


FIGURE 9.5 Effect of the confining pressure: Experimental and numerical “shear stress–displacement” diagrams of a small confined wall under shear loading conditions.

Simulation of a confined medium-sized masonry panel under shear loading conditions

In the case of confined masonry panels subjected to shear loads with various confining stresses ($\sigma = 0.4, 0.6, 0.8,$ and 1.2 MPa), the joint response differs from that observed under nonconfined conditions, as shown in Fig. 9.5. Experimental results are plotted in dashed lines. In the “stress–displacement” diagrams, the distinction will be made between three stresses, τ_c , τ_u , and τ_{cr} (see Fig. 9.6; Rezik and Lebon, 2010, available for nonconfined masonry structures), where τ_{cr} denotes the end of the softening phase.

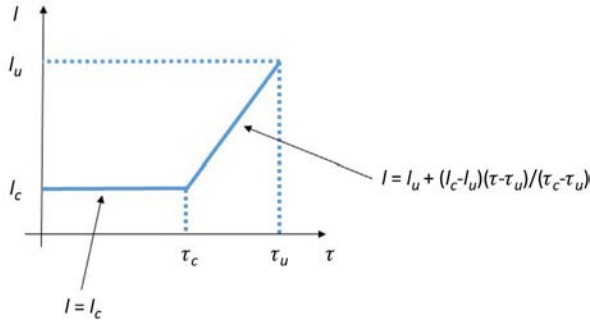


FIGURE 9.6 Function describing the evolution of the crack half-length with respect to the shear stress applied: the case of a triplet of hollow bricks (Rekik and Lebon, 2010), a nonconfined seven brick structure and that of a wall.

Additional confining pressure was found to increase the cohesion between mortar and hollow bricks and thus to induce the occurrence of softening and sliding processes after the peak load has been reached. These softening and sliding parts cannot be modeled in the framework of a crack-length evolution law similar to that used for a nonconfined masonry panel (Figs. 9.5 and 9.6; Rekik and Lebon, 2010). In this case, a nonlinear piecewise increasing representative crack length from the peak load up to failure gives better predictions. To obtain a better fit between the numerical and experimental data, the crack lengths were identified at several points on the experimental diagram. At various confining stresses, the changes in the crack lengths given in Fig. 9.7 show that it is necessary to include a bilinear or trilinear function in the postpeak load part to account for the set of the softening and sliding parts. As shown in Fig. 9.7, these functions describe the increase in the crack length, while the shear stress decreases, in line with the properties of cohesive cracks (Park et al., 2008; Chaimoon and Attard, 2009). In the identified functions $l = f(\tau)$ corresponding to confining stresses $\sigma = 0.8$ and 1.2 MPa, note the existence of a first positive slope describing the increase in the crack length with the increase in the shear stress occurring before the peak of load is reached. This first linear evolution of l is not included in the description of the crack-length evolution in the softening and sliding parts given by the “stress–displacement” diagrams.

The numerical “stress–displacement” curves corresponding to the crack-length functions depicted in Fig. 9.7 are in line with experimental data as can be seen from Fig. 9.5 with each of the confining stresses. Table 9.2 lists the ultimate crack lengths obtained at the various confining pressures tested. Note that the crack length l_u varies slightly with the confining pressure. Its main value is $l_u^{cp} = 6.46 \times 10^{-2} \mu\text{m}$. The relative errors e_r between l_u and the average value l_u^{cp} do not exceed 11%.

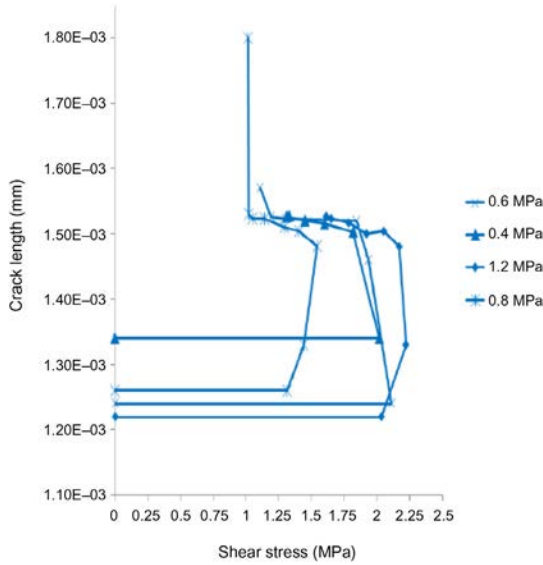


FIGURE 9.7 Identified crack-length laws giving the best fit between experimental and numerical data on confined small walls under shear loads and various confining pressures.

TABLE 9.2 Identified ultimate representative crack length and the corresponding relative errors obtained on small confined walls under shear loading and different confining pressures.

Confining stress, σ (MPa)	l_u (μm)	$e_r(l_u)$ (%)
0.4	6.22×10^{-2}	2.5
0.6	5.98×10^{-2}	5.0
0.8	7.63×10^{-2}	11.1
1.2	5.98×10^{-2}	5.0

Fig. 9.8 gives the local shear stress distribution with a 0.4 MPa confined small wall, which shows a local stress concentration at the longest vertical interface v_1 , where the decohesion between brick and mortar mainly occurs, as in the experimentally tested specimen (Fig. 9.9). Fig. 9.8 gives the local shear stress distribution with a 0.4 MPa confined small wall, which shows a local stress concentration at the longest vertical interface v_1 , where the decohesion between brick and mortar mainly occurs, as in the experimentally tested specimen (Fig. 9.9).

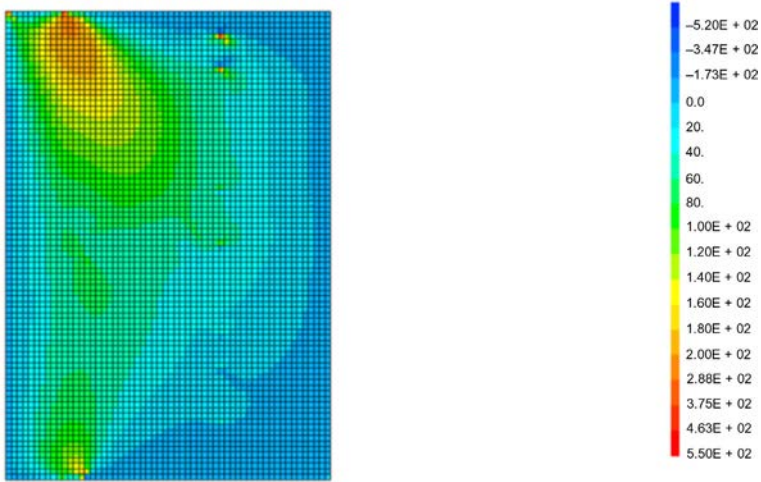


FIGURE 9.8 Local shear stress snapshot of a confined small wall ($\sigma = 0.4$ MPa) under shear loading conditions at failure (the identified ultimate crack length is $l = 6.22 \times 10^{-2}$ μm).

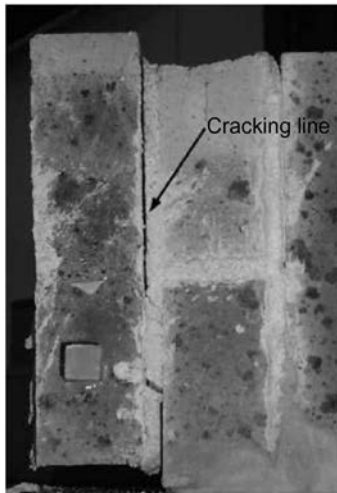


FIGURE 9.9 Experimental deformation of a small confined wall under shear loading conditions. From Gabor, A., Bennani, A., Jacquelin, E., Lebon, F., 2006. Modelling approaches of the in-plane shear behavior of unreinforced and FRP strengthened masonry panels. *Comput. Struct.* 74, 277–288.

Discussion of the results

Table 9.3 recapitulates the identified ultimate crack lengths giving a best fit between the numerical and experimental results at the failure of the wall with and without the unilateral contact condition. The relative difference

TABLE 9.3 Identified ultimate representative crack length and the corresponding relative errors obtained on a diagonally compressed wall with and without a unilateral contact condition.

Unilateral contact condition	$l_u(\mu\text{m})$	$e_r(l_u)(\%)$
With	6.46×10^{-2}	3
Without	7.18×10^{-2}	4

TABLE 9.4 Relative errors in the identified (average) ultimate representative crack lengths and stiffnesses in the case of masonries of various sizes under shear loading or diagonal compression conditions.

	l_u or average of $l_u(\mu\text{m})$	$e_r(l_u)(\%)$	$e_r(C_N)(\%)$
Nonconfined prism	5.86×10^{-2}	5.8	+ 17.4
Confined prism	6.46×10^{-2}	0.6	- 2.0
Wall (with/without u.c.c.)	6.76×10^{-2}	3.7	- 11.0

between these values is taken to be negligible (about 7%). It was therefore proposed to calculate the mean ultimate crack length from the values available on wall interfaces at failure. The relative errors e_r between the identified crack lengths l_u and the mean value $l_u^w = 6.64 \times 10^{-2} \mu\text{m}$ obtained in the case of the wall were negligible (below 4%).

Table 9.4 gives the identified (average) ultimate crack lengths obtained with masonry structures of various sizes under shear loads (with and without confining pressure) or diagonal compression loads (with and without the unilateral contact condition). Due to the negligible differences existing between these values, we will assume that failure occurs when the crack length reaches the average value of this set of identified crack lengths, that is, $l_u = 6.4 \times 10^{-2} \mu\text{m}$.

In the case of masonry composed of constituents with the properties given in Table 9.1, comparisons between the stiffnesses of the interfaces obtained with masonry of various sizes (see the values for the stiffnesses) give a mean stiffness value per mm, with upper and lower bounds for the properties thus identified:

$$\left\{ \begin{array}{l} C_N^{av} = 2.52 \times 10^{11} \left(\frac{N}{\text{mm}^3} \right) \quad \text{and} \quad C_T^{av} = 1.42 \times 10^{11} \left(\frac{N}{\text{mm}^3} \right) \\ (1 - 11\%)C_N^{av} \leq C_N \leq (1 + 17\%)C_N^{av} \end{array} \right. \quad (9.14)$$

The discrepancies between the individual interface stiffnesses and the mean value obtained (maximum of 17%) can be explained by the fact that masonry mortar joints are manmade materials.

9.2.1.5 Conclusions

The identification of the crack-length evolution law for masonry structures with various sizes subjected to shear and diagonal compression (Rekik and Lebon, 2010) loads showed the ability of a recently presented model (Rekik and Lebon, 2010, 2012) to provide estimations for the stiffness of masonry interfaces. At failure, the discrepancies between the identified crack lengths were almost negligible (below 6%). The interface stiffnesses are inversely proportional to the square of the ultimate crack length l_u , which explains the maximum discrepancy of about 17%. An experimental campaign in which the joint mortar is consistently prepared and laid (constant thickness, regular rate of cover between brick and mortar) will help to reduce the discrepancies between the stiffnesses of interfaces at failure. To obtain a good fit between experimental and numerical data on loaded nonconfined masonry structures in which the “stress–strain” diagrams show the occurrence of a “plateau” after the peak load (or stress), it is necessary to adopt a linearly increasing crack length up to the failure, corresponding to the ultimate load applied. The number of parameters is reduced to 4 in this case: l_c , l_u , c , and u . In the case of confined masonry structures under shear loading conditions, the present model gives good agreement with the experimental data, thanks to the introduction of a bilinear or trilinear function describing the increase in the crack length with the decrease in the shear stress in the postpeak part (softening and sliding parts). The number of parameters increases in this case to 6 or 8. In the postpeak part of the “stress–displacement” diagram, a single linear function describing the increase in the crack length with the decrease in the shear stress does not suffice to reproduce accurately the softening and sliding parts.

9.2.2 Accounting for creep of masonry components

The recent collapse of famous historical constructions (e.g., middle-age masonry buildings) was mainly attributed to the creep behavior of the masonry (Binda et al., 1992; Shrive et al., 1997; Papa and Taliercio, 2005). Recent experimental findings have shown that the accumulation of creep-induced damage in time under sustained loads is a possible reason for this collapse. Thus, in order to increase the performance and safety of refractory linings and ancient masonry buildings subjected to heavy sustained loading, the development of theoretical models of creep evolution and creep-induced damage is of crucial importance. In Choi et al. (2007), an experimental study was carried out to investigate the creep of masonry. Different rheological

models are considered to assess their ability to predict the creep of masonry. Accordingly, it was found that the Modified Maxwell (MM) model is the most accurate one. On the other hand, these materials (e.g., refractory linings, masonries) are generally heterogeneous and composed of bricks and mortar joints. Therefore, the evaluation of their response requires homogenization approaches. In this connection, the so-called hereditary approaches based on Stieltjes convolution in the time domain has been used by many authors for modeling linear nonaging viscoelastic composites. Two steps are performed. First, through the use of the Laplace–Carson (LC) transform with the correspondence principle (Mandel, 1966), the time-dependent constitutive relations of the local phase properties are converted into symbolic elastic-like relations in the LC domain. Then, the symbolic macroscopic elastic moduli of the fictitious elastic material are derived by using classical elastic micromechanical schemes such as the self-consistent (SC) scheme (Hashin, 1969; Rougier et al., 1994), the Mori–Tanaka estimate (Li and Weng, 1994; Pichler and Lackner, 2009), or the Hashin–Shtrikman bounds (De Botton and Tevet-Deree, 2004). Finally, the overall properties of the viscoelastic composites in the physical domain are obtained by LC inversion, which can be performed either analytically or numerically. However, apart from some particular cases (Rougier et al., 1994), the inversion of the LC transform is usually performed numerically (see, e.g., the collocation method; Schapery, 1962). Moreover, the analytical method based on the Bromwich integral defined in the complex plane as shown in Beurthey and Zaoui (2000) leads most of the time to integral equations over the whole loading path even if the different phases of the heterogeneous composite exhibit limited memory effects. This last point makes difficult direct extensions to more general situations (e.g., thermomechanical loading, aging viscoelasticity). Moreover, these methods require the complete past history of stress and strain. To overcome these limitations, a number of theories have been proposed in the past aiming to formulate incremental constitutive equations for the linear viscoelastic behavior. Among them, researchers Dubois et al. (1999), Kim and Sing Lee (2007), and Chazal and Moutu Pitti (2009) proposed the incremental formulation and constitutive equations in the finite element (FE) context. In fracture mechanics of viscoelastic materials, Dubois et al. (2002) and Nguyen et al. (2010) applied the incremental formulation in order to evaluate the crack growth process in wood and concrete, respectively. Concerning combined damage and creep effects for masonry within the framework of homogenization, it is worth noting that in the literature there are few works devoted to these studies. For instance, Brooks (1990) obtained the creep coefficients of brickwork according to the properties of the individual constituents. Cecchi and Tralli (2012) adopted an asymptotic homogenization procedure for the derivation of the creep behavior of uncracked periodic masonry cell with joints of finite dimensions. For uncracked masonry, Cecchi and Taliercio (2013) compared predictions given

by a simplified analytical model and a more accurate FE model, both based on homogenization procedures. Nguyen et al. (2011) derived the effective behavior of microcracked linear viscoelastic concrete obeying the Burgers model by performing a combination of Griffith's theory (Huy Duong, 1978) and the Eshelby-based homogenization scheme (Bornert and Suquet, 2001; Deudé et al., 2002). This model does not rest on a series expansion such as the widely used Prony–Dirichlet series or the collocation method and its extensions (the multidata method (Cost and Becker, 1970) or the optimized collocation method (Rekik and Brenner, 2011)) for the required temporal functions. Indeed, as the uncracked concrete, the microcracked concrete was assumed to obey the Burgers model. The FE homogenization method classically used for uncracked elastic or viscoelastic masonries is extended here to microcracked viscoelastic masonry.

9.2.2.1 *Main objective and hypothesis*

The objective of this section is to evaluate at each time t the effective and local behavior of masonries exhibiting nonlinear behaviors, mainly viscoelastic at short and/or long times especially when subjected to severe or long-term loading such as historical monuments or refractory masonry linings working under high temperatures. For the sake of simplicity, it can be assumed that only the mortar is a microcracked viscoelastic material (Luciano and Sacco, 1997; Sacco, 2009). Its behavior (at the uncracked state) obeys the MM rheological model. Blocks or bricks are assumed to be uncracked and to have either rigid or elastic isotropic behavior. In the mortar, the cracks are assumed to be penny-shaped and to have an isotropic distribution. The proposed approach is based on three main steps. First, the homogenization technique is applied in order to assess the effective behavior of the nonaging microcracked mortar. The results of brittle fracture mechanics—Griffith's theory—could be useful if we move from the real temporal space to the symbolic one due to the LC transform. In the latter space, the apparent behavior of the mortar is linear elastic. This procedure allows the use of expressions available in the literature for the displacement's jump induced by the crack (Nguyen et al., 2011). Assuming again that the displacement jump field depends linearly on the macroscopic stress, it is possible to define an effective linear behavior for the microcracked mortar in the symbolic space. To determine the global behavior in the real space time, it is possible to apply the inverse of the LC transform in some simple cases. It is then interesting to approach in the symbolic space, at least in short and long terms, the symbolic effective stiffness (or compliance) by an existing rheological model. For example, if the uncracked mortar behaves as the MM model, we can try to approach the symbolic effective behavior of the corresponding microcracked mortar by the same model. After validation of this approximation at short and long terms, the inversion of the apparent effective

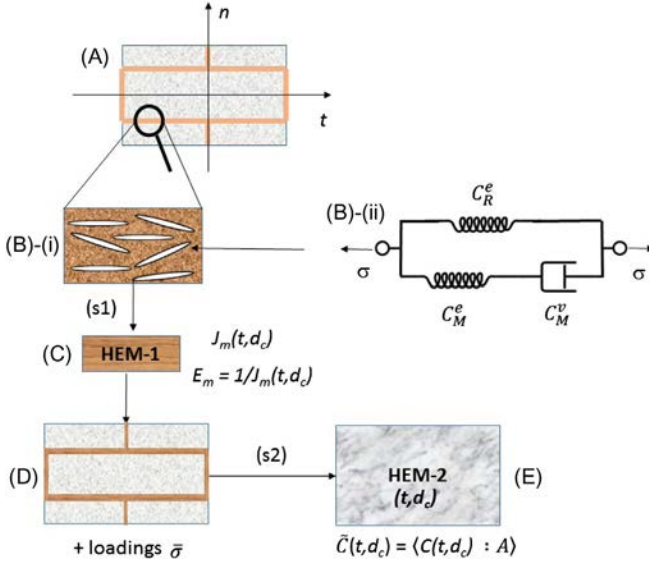


FIGURE 9.10 Main steps of the proposed FE model: The first one (s1) relies on the coupling between Griffith’s brittle fracture theory and stress-based dilute homogenization scheme defining the homogeneous material HEM-1 (C) equivalent to the microcracked linear nonaging viscoelastic mortar (B)-(i) joints present in the periodic masonry cell (A). At each time and for every crack density d_c , the second step (s2) provides the effective stiffness of the homogeneous material HEM-2 (E) equivalent to the masonry’s periodic cell (D). Here, the rheology of the mortar with penny-shaped microcracks follows the Modified Maxwell (B)-(ii) model.

stiffness will be straightforward. Therefore, the effective creep behavior of the microcracked viscoelastic mortar could be expressed in the real space time. This first step permits us to determine fast and easily temporal bulk and shear moduli of mortar as explicit functions of the crack density parameter (Budiansky and O’Connell, 1976; Dormieux et al., 2006). For the proposed model in this section, the second step relies either on FE homogenization of the periodic masonry cell (see step s2) in Fig. 9.10 when considering the FE “direct” method. Basic steps followed by the proposed FE model are summarized in Fig. 9.10.

9.2.2.2 Creep model for microcracked mortar (step 1)

The rate-dependent mechanical behavior of mortar is often approximated by a linear viscoelastic model (Choi et al., 2007; Ignoul et al., 2007). For the sake of simplicity, only nonaging formulation will be considered in this work. The practical interest of this simple formulation is that it allows us to

transform a time-dependent boundary value problem into a linear elastic one using the well-known correspondence theorem based on the LC transform. Among the simplest formulations used to model the nonaging linear viscoelastic mortar's behavior, it is possible to quote the Ross, Feng, Burgers, and MM models (Choi et al., 2007; Cecchi and Tralli, 2012) mainly based on connections in parallel and/or in series of Maxwell (M) and Kelvin–Voigt (KV) parts. Each element (spring and dashpot) of the M or KV model is characterized by an isotropic fourth-order tensor related to its elasticity or viscosity:

$$\begin{aligned} C_{KV}^e &= 3k_{KV}^e J + 2\mu_{KV}^e K, & C_{KV}^v &= \eta_{KV}^s J + \eta_{KV}^d K \\ C_M^e &= 3k_M^e J + 2\mu_M^e K, & C_M^v &= \eta_M^s J + \eta_M^d K \end{aligned} \quad (9.15)$$

where k_α and μ_α ($\alpha = KV$ or M) denote the bulk and shear moduli and η_α^s and η_α^d represent the bulk and shear viscosities, respectively. The tensors J and $K = I - J$ are the usual projectors on the subspaces of purely spherical or deviatoric second-order tensors, and i and I are second- and fourth-order identity tensors. In the following, only the MM model is considered since it has been demonstrated in Choi et al. (2007) and Rekić et al. (2016) that this rheological model is relevant at short and long terms for the masonry. The constitutive law of the MM's model (see Fig. 9.10B-(ii)) is given by:

$$S_M^v \sigma + S_M^e \cdot \sigma = S_M^v C_R^e \varepsilon + (I + S_M^e C_R^e) \cdot \varepsilon \quad (9.16)$$

where for isotropic mortar material, the elastic and viscous compliances of the Maxwell part are given respectively by:

$$S_M^e = \frac{1}{3k_M^e} J + \frac{1}{2\mu_M^e} K \text{ and } S_M^v = \frac{1}{\eta_M^s} J + \frac{1}{\eta_M^d} K \quad (9.17)$$

The elastic stiffness of the spring reads $C_R^e = 3k_R^e J + 2\mu_R^e K$. The LC transform applied to the behavior law (9.16) leads to:

$$(S_M^v + pS_M^e) \sigma^* = (S_M^v C_R^e + p(I + S_M^e C_R^e)) \varepsilon^* \quad (9.18)$$

and allows the definition of the following symbolic MM elastic compliance:

$$S_{MM}^* = (S_M^v C_R^e + p(I + S_M^e C_R^e))^{-1} ((S_M^v + pS_M^e)) \quad (9.19)$$

Recall that the LC transform of a temporal function $f(t)$ is given by $F(p) = p \int_0^\infty e^{-pt} f(t) dt$. p is the variable that replaces time t in the symbolic LC space. Assuming the isotropy of the mortar behavior, the symbolic compliance (9.19) reads:

$$S_{MM}^* = \frac{1}{3k_s^*} J + \frac{1}{2\mu_s^*} K \quad (9.20)$$

The associated apparent creep function is then given by:

$$J_{MM}^* = \frac{1}{E_{MM}^*} = \frac{1}{9k_s^*} + \frac{1}{3\mu_s^*} = \frac{1}{9 \left(k_R + \frac{pk_M\eta_M^s}{k_M + \frac{p\eta_M^s}{2}} \right)} + \frac{1}{3 \left(\mu_R + \frac{p\mu_M\eta_M^d}{\mu_M + \frac{p\eta_M^d}{2}} \right)} \quad (9.21)$$

The analytical direct inversion of (9.21) leads to the MM real creep function:

$$J_{MM}(t) = \frac{1}{9k_R} + \frac{1}{3\mu_R} - \frac{k_M}{9k_R(k_R + k_M)} e^{-t/\tau_{MM}^s} - \frac{\mu_M}{3\mu_R(\mu_R + \mu_M)} e^{-t/\tau_{MM}^d} \quad (9.22)$$

with the characteristic times $\tau_{MM}^s = \eta_M^s(k_R + k_M)/3k_Rk_M$ and $\tau_{MM}^d = \eta_M^d(\mu_R + \mu_M)/2\mu_R\mu_M$ for the spherical and deviatoric parts of the MM viscous behavior, respectively.

9.2.2.3 Microcracked mortar: Modified Maxwell model parameters

This section provides elastic and viscous coefficients for a microcracked mortar following the MM rheological model. The identification procedure of these parameters, which represents step 1 of the proposed FE model, is detailed in Rezik et al. (2016).

$$\begin{aligned} k_R(d_c) &= \frac{k_R}{(1 + d_c Q_0^0)}, & \mu_R(d_c) &= \frac{\mu_R}{1 + d_c M_0^0} \\ k_M^e(d_c) &= \frac{(k_M + k_R)}{(1 + d_c Q_0^\infty)} - \frac{k_R}{(1 + d_c Q_0^0)}, & \mu_M(d_c) &= \frac{\mu_M + \mu_R}{1 + d_c M_0^\infty} - \frac{\mu_R}{1 + d_c M_0^0} \\ \eta_M^s(d_c) &= \frac{(\eta_M^s + d_c(\eta_M^s Q_0^0 - 3k_R^e Q_0^1))}{(1 + d_c Q_0^0)^2}, & \eta_M^d(d_c) &= \frac{\eta_M^d + d_c(\eta_M^d M_0^0 - 3\mu_R M_0^1)}{(1 + d_c M_0^0)^2} \end{aligned} \quad (9.23)$$

where

$$\begin{aligned}
Q_0^0 &= \frac{4k_R^s(3k_R + 4\mu_R)}{3\mu_R(3k_R + \mu_R)}, \\
Q_0^1 &= \frac{2(2\eta_M^s\mu_R - 3k_R\eta_M^d)(9k_R^2 + 4\mu_R^2 + 6k_R\mu_R)}{9 \cdot 3\mu_R^2(3k_R + \mu_R)^2} \\
M_0^0 &= \frac{16(3k_R + 4\mu_R)(9k_R + 4\mu_R)}{45(3k_R + \mu_R)(3k_R + 2\mu_R)}, \\
M_0^1 &= \frac{8(3k_R\eta_M^d - 2\eta_M^s\mu_R)(63k_R^2 + 16\mu_R^2 + 60k_R\mu_R)}{45 \cdot 3\mu_R^2(3k_R + \mu_R)^2} \\
Q_0^\infty &= \frac{4}{3}(k_M + k_R) \left(\frac{1}{\mu_M + \mu_R} + \frac{3}{3(k_M + k_R) + (\mu_M + \mu_R)} \right) \\
M_0^\infty &= \frac{16}{45}(k_M + k_R) \left(\frac{9(k_M + k_R)}{3(k_M + k_R) + (\mu_M + \mu_R)} - \frac{6(k_M + k_R)}{3(k_M + k_R) + 2(\mu_M + \mu_R)} \right)
\end{aligned} \tag{9.24}$$

The approximate creep function of a microcracked mortar matrix that follows the MM model reads:

$$\begin{aligned}
J_{MM}^{app}(t, d_c) &= \frac{1}{k_R(d_c)} \left(1 - \frac{k_M(d_c)}{(k_R(d_c) + k_M(d_c))} e^{-\frac{t}{\tau_{MM}^s(d_c)}} \right) \\
&\quad + \frac{1}{3\mu_R(d_c)} \left(1 - \frac{\mu_M(d_c)}{(\mu_R(d_c) + \mu_M(d_c))} e^{-\frac{t}{\tau_{MM}^d(d_c)}} \right)
\end{aligned} \tag{9.25}$$

where here the characteristic times of the spherical and deviatoric parts of the MM model are, respectively: $\tau_{MM}^s(d_c) = \eta_M^s(d_c)(k_R(d_c) + k_M(d_c))/3k_R(d_c)k_M(d_c)$ and $\tau_{MM}^d(d_c) = \eta_M^d(d_c)(\mu_R(d_c) + \mu_M(d_c))/2\mu_R(d_c)\mu_M(d_c)$.

9.2.2.4 Principle of the finite element homogenization of a microcracked viscoelastic masonry periodic cell (step 2)

Instead of differentiating the mortar's constitutive law as it can be done when considering an incremental homogenization approach (Nguyen et al., 2010), it is easier and more practical to consider the approximate mortar's creep function (9.25) identified at the short and long terms, which is an explicit function of time and crack density parameter. Therefore, there is no prestress in the considered viscoelastic mortar. At each time t , the behavior of the viscoelastic phase r can be considered to be "purely elastic" with a

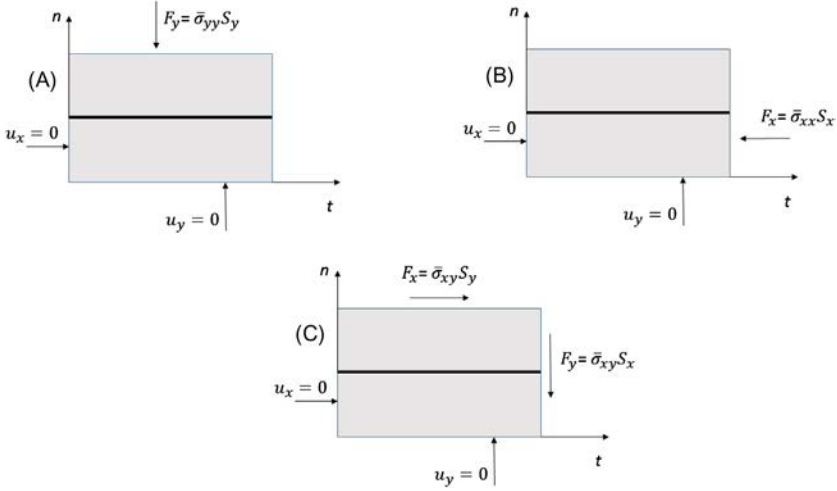


FIGURE 9.11 Boundary and symmetry conditions for the considered quarter cell subjected to axial normal (A) or tangential (B) compression or shear (C) loadings.

constant Poisson's ratio and Young's modulus $E^r(t, d_c) = 1/J^r(t, d_c)$ if damaged or $E^r(t) = 1/J^r(t)$ otherwise. When applying a constant macroscopic stress and assuming that the per phase localization tensor A^r is time-independent following the hypothesis of Deudé et al. (2002) then the average strain $\bar{\varepsilon}^r$ per phase r and the masonry overall behavior reduce, respectively, to $\bar{\varepsilon}^r = A^r : \bar{\varepsilon}$ and $\bar{\sigma} = \tilde{C} : \bar{\varepsilon}$, where the overall tangent stiffness is given by $\tilde{C} = \langle C : A \rangle$ and the average strain localization over the periodic cell reads $\langle A \rangle = I$. It is then important to determine components of the localization strain tensor A^r_{ijkl} . Since regular masonry presents periodic microstructure, it is possible to consider only a periodic cell as shown in Fig. 9.11A. Moreover, as the periodic cell presents two axes of symmetry, normal and tangential directions along the unit vectors n and t , respectively, only its quarter (see Fig. 9.11B) will be retained for computation. To assess the effective “elastic engineering constants,” it is proposed to subject the unit cell to three types of loadings: axial compression along n , axial compression along t , and shear loading, as shown in Fig. 9.10. In this case, strain localization components A^r_{ijkl} are given by the following equations:

$$\begin{aligned}
 \bar{\varepsilon}^r_{xx} &= A^r_{xyyy} \bar{\varepsilon}_{yy}, & \bar{\varepsilon}^r_{yy} &= A^r_{yyyy} \bar{\varepsilon}_{yy} & \text{for } \bar{\varepsilon} &= \bar{\varepsilon}_{yy} e_y \otimes e_y \\
 \bar{\varepsilon}^r_{xx} &= A^r_{xxxx} \bar{\varepsilon}_{xx}, & \bar{\varepsilon}^r_{yy} &= A^r_{yyxx} \bar{\varepsilon}_{xx} & \text{for } \bar{\varepsilon} &= \bar{\varepsilon}_{xx} e_x \otimes e_x \\
 \bar{\varepsilon}^r_{xy} &= 2A^r_{xyxy} \bar{\varepsilon}_{xy}, & & & \text{for } \bar{\varepsilon} &= \bar{\varepsilon}_{xy} (e_x \otimes e_y + e_y \otimes e_x)
 \end{aligned} \tag{9.26}$$

Note that the localization strain tensor A^r is assumed to be orthotropic. Since the symmetry of the Cauchy strain tensor both in the anisotropic and isotropic spaces is required, it follows that $A_{ijkl}^r = A_{jikl}^r = A_{jilk}^r$ (minor symmetry). The major symmetry of A^r is also necessary $A_{ijkl}^r = A_{klji}^r$. It follows that only the components A_{xxxx} , A_{yyyy} , $A_{xyxy} = A_{xyyx}$ and $A_{yxyx} = A_{yxxy}$ are not null. According to the classical Voigt notation, the constitutive behavior law $\bar{\sigma} = \tilde{C}:\bar{\varepsilon}$ of the unit cell reads:

$$\begin{pmatrix} \bar{\sigma}_{yy} \\ \bar{\sigma}_{xx} \\ \bar{\sigma}_{xy} \end{pmatrix} = \begin{pmatrix} \tilde{C}_{nnnn} & \tilde{C}_{mntt} & 0 \\ \tilde{C}_{mntt} & \tilde{C}_{tttt} & 0 \\ 0 & 0 & \tilde{C}_{nnnt} \end{pmatrix} \begin{pmatrix} \bar{\varepsilon}_{yy} \\ \bar{\varepsilon}_{xx} \\ 2\bar{\varepsilon}_{xy} \end{pmatrix} \quad (9.27)$$

where $\bar{\sigma} = \langle \sigma \rangle_V$ is the overall applied stress on the periodic cell. The software Cast3M has been used to provide local mechanical fields and mainly average mechanical fields such as strain $\bar{\varepsilon}^r$, stress $\bar{\sigma}^r$ over each phase r ($r=b$ for bricks, m for mortar), and macroscopic strain $\bar{\varepsilon} = \sum_{r=m,b} f^r \bar{\varepsilon}^r$ calculated in order to deduce components of the effective tangent stiffness \tilde{C} (Eq. 9.27). The five engineering ‘‘constants’’ are then given by:

$$\begin{aligned} \frac{1}{\tilde{E}_n(t, d_c)} &= \frac{\tilde{C}_{nnnn}}{\tilde{C}_{tttt}\tilde{C}_{nnnn} - \tilde{C}_{ttnn}\tilde{C}_{nnnt}}, & \frac{1}{\tilde{E}_m(t, d_c)} &= \frac{\tilde{C}_{tttt}}{\tilde{C}_{tttt}\tilde{C}_{nnnn} - \tilde{C}_{ttnn}\tilde{C}_{mntt}} \\ \tilde{\mu}_{nt}(t, d_c) &= \tilde{C}_{nnnt}, & \tilde{\nu}_{nt}(t, d_c) &= \frac{\tilde{C}_{mntt}}{\tilde{C}_{tttt}}, & \tilde{\nu}_m(t, d_c) &= \frac{\tilde{C}_{ttnn}}{\tilde{C}_{nnnn}} \end{aligned} \quad (9.28)$$

Recall that for an isotropic material (brick and mortar), components of the stiffness tensor C_r ($r = b, m$) read:

$$C_{xxxx}^r = C_{yyyy}^r = k^r + \frac{4}{3}\mu^r, \quad C_{xxyy}^r = C_{yyxx}^r = k^r - \frac{2}{3}\mu^r, \quad C_{xyxy}^r = 2\mu^r \quad (9.29)$$

where $k^r = (E/3(1 - 2\nu))$ and $\mu^r = (E/2(1 + \nu))$ are the bulk and shear moduli, respectively.

9.2.2.5 Time-dependent crack density and first application of the proposed model

Time-dependent crack density

Various damage models are described in the literature (Lemaitre, 1996; Garavaglia and Lubelli, 2002; Sukontasukkul et al., 2004). Here, for the sake of simplicity and as a first approach we have chosen for the microcracked masonry a simple damage evolution model following

Reda Taha and Shrive (2006) and Shrive and Reda Taha (2008). According to these papers, accumulated damage is assumed to follow Weibull's failure rate function such that:

$$d_c(t) = \sum_{t_0}^{t_1} \frac{100\eta}{\tau_D} \left(\frac{t}{\tau_D} \right)^n \quad (9.30)$$

where τ_D is a constant damage time that refers to the time where most damage would occur. This damage not related to externally applied loads can be induced by external or internal effects such as freeze-thaw, alkali-silica reaction, sulfate-attack, etc. This load-independent model is consistent with Verstryngne et al. (2009) and Garavaglia et al. (2004) who showed that the Weibull failure rate function could be used successfully to predict the failure of masonry. As a first approach and according to a damage scenario considered by Shrive and Reda Taha (2008), the coefficients are taken here as $\tau_D = 800$ (days), $\eta = 0.3$ (days), and $n = 10$. $d_c(t)$ represents the level of damage accumulated from the time at which damage starts, t_0 , to the time of evaluation. In the calculations here, damage is assumed to begin at 400 days. The rate of damage accumulation with this model is slow initially, but accelerates over time, as shown in Fig. 9.12 reporting Figure 4.4 in Shrive and Reda Taha (2008). Quite considerable damage is assumed to occur in a relatively short time in this example. Here, the damage factor attains about 0.33 after 1000 days with the damage starting at 400 days. Other possible damage scenarios or sophisticated accumulated damage functions accounting for both external applied loading and time parameters as that available for rockslat material developed by Chan et al. (1992) could be used in future investigations. As shown hereafter, Eq. (9.30), the only time-dependent model, is a starting point allowing first assessments of the proposed FE model.

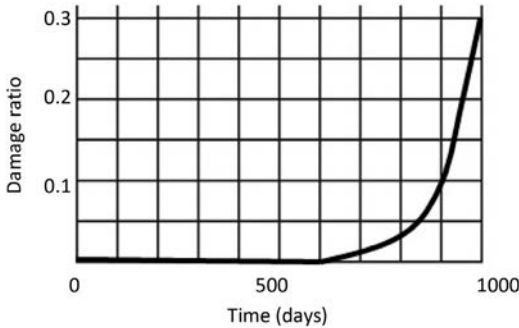


FIGURE 9.12 Nonlinear evolution of damage ratio with time. *From Shrive, N.G., Reda Taha, M.M., 2008. Effects of creep on new masonry structures. In: Binda, L. (Ed.), Learning from Failure – Long-Term Behaviour of Heavy Masonry Structures. WIT Press, pp. 83–108.*

Case of a periodic unit cell: comparisons at short and long terms

In this section, it is proposed to investigate trends of evolutions with the time of overall predictions of a periodic masonry cell provided by the proposed FE model and their sensitivity to mortar joint thickness and brick dimensions (height and width). Microcracked mortar is assumed to follow the generalized Maxwell (GM) model. Here, for the sake of simplicity, only one term is considered for the GM model. Accordingly, the rheological model followed by the mortar's behavior coincides with the MM's model. In this study, bricks are assumed to be either rigid ($E_b = 1000E_m(t=0)$) or elastic ($E_b = 2.22E_m(t=0)$) and uncracked with a Poisson's ratio $\nu_b = 0.15$. Bricks are 250 mm thick. Their dimensions in the plane (x, y) are the following: height $a = 55$ mm and width $b = 120$ mm. The mortar joint's thickness is $th = 10$ mm. For the viscous rheological model, since the instantaneous Young's modulus E_0 for the MM model is given by $E_m(t=0) = E_R + E_M$, where the relaxation modulus is set equal to $E_M = e_i E_0$, the spring's Young's modulus E_R reads $E_R = (1 - e_i)E_0$. Here, e_i is a dimensionless parameter. All the ensuing computations have been carried out under the plane stress assumption by using a quadratic element "QUA8" with eight nodes and a refined mesh comprised of 10,336 elements using the software Cast3M. This fine mesh is chosen because it provides accurate effective results. Since we are studying the masonry creep phenomenon, we apply instantaneously a constant force at selected points of the boundary (i.e., a sustained macroscopic stress) as shown in Fig. 9.10. Hereafter, for a mortar joint thickness $th = 10$ mm and properties identified at short (Table 9.5) and long terms (Table 9.6), time evolutions of effective tangent creep coefficients

TABLE 9.5 Elastic and viscous moduli of a mortar identified at the short term and tested by Brooks (1990) and Cecchi and Taliercio (2013).

	E_0 (MPa)	ν_m	e_i	$e_r(I_u)$ (%)
Mortar	7700	0.2	0.7602	7.1

TABLE 9.6 Elastic and viscous moduli of hybrid mortar gathered at the long term.

E_M (MPa)	τ_M (s)	E_R (MPa)	τ_R (s)	ν_m
4000	2×10^8	2112	300,000	0.29

Source: From Verstryne, E., Ignoul, S., Schueremans, L., Gemert, V.D., 2008. Modelling of damage accumulation in masonry subjected to a long-term compressive load. In: d'Ayala, D., Fodde, E. (Eds.), Structural Analysis of Historic Construction. CRC Press, pp. 525–532 (Verstryne et al., 2008).

provided by the FE model for masonries with rigid bricks and cracked mortar with a crack density evolving according to (Eq. 9.30) are reported in Fig. 9.13. Table 9.7 shows the decrease with increasing time and crack density of mortar's Young's moduli either for short- or long-term identified properties.

FE predictions: As a whole, it is observed that FE predictions for masonry's effective tangent moduli decrease with the increase of time. This can be explained by the increase of the damage level with time as illustrated in Fig. 9.12. For masonry with short-term mortar properties and either elastic (Fig. 9.14, Rekik et al., 2016) or rigid (Fig. 9.4) bricks, effective moduli

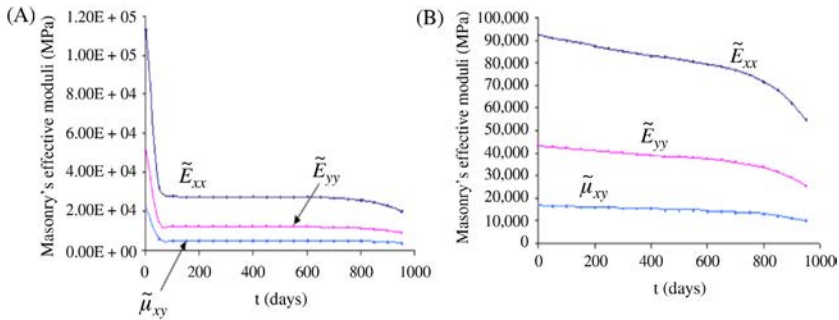


FIGURE 9.13 FE predictions for effective tangent moduli of masonry with rigid bricks ($E_b = 1000E_m$ ($t = 0$)), joints thickness $th = 10$ mm, and mortar parameters identified at short (A) and long terms (B).

TABLE 9.7 Mortar Young's moduli for different crack densities evolving due to the law (Eq. 9.30).

t (days)	d_c	E_j (short term) (MPa)	E_j (long term) (MPa)
0	0	7700	6112
50	3.41×10^{-14}	2148	6027
150	2.01×10^{-9}	1855	5866
350	9.63×10^{-6}	1846	5575
450	1.19×10^{-4}	1846	5441
650	4.70×10^{-3}	1831	5159
750	1.96×10^{-2}	1784	4923
850	6.87×10^{-2}	1645	4454
900	1.217×10^{-1}	1517	4074
950	2.10×10^{-1}	1345	3581

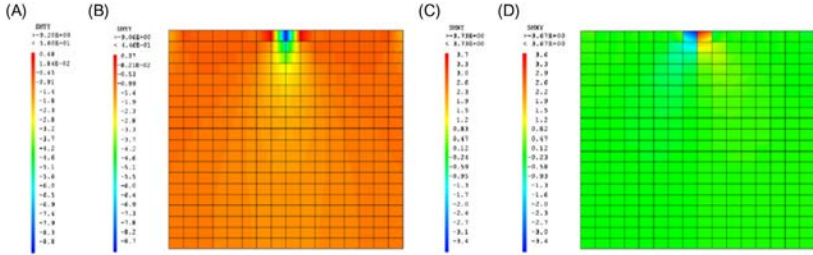


FIGURE 9.14 Comparisons at time $t = 900$ days of CTR (A and C) and FE (B and D) predictions for stress snapshots (σ_{yy} (A and B), σ_{xy} (C and D)) in the compressed wall with rigid bricks $E_b = 1000E_m$ ($t = 0$) and mortar’s properties identified at the long term.

decrease significantly during the first 50 days. This is consistent with the significant decrease of the mortar’s Young’s modulus as illustrated in Table 9.7 (column “short term”). After almost 100 days, the decrease of effective moduli is slow as observed for the case of masonry with long-term mortar properties throughout the whole period considered ($[0, 950]$ (days)). Moreover, masonries with rigid bricks ($E_b = 1000E_m$ ($t = 0$)) show pronounced anisotropy compared to those with elastic bricks ($E_b = 2.22E_m$ ($t = 0$)) for which effective Young’s moduli \tilde{E}_{xx} and \tilde{E}_{yy} are close mainly at the long term, see Fig. 9.14B (Rekik et al., 2016). Hereafter, only the time range $[600, 950]$ (days) is considered since the crack density is almost negligible for the time period $[0, 600]$ (days) (see Table 9.7). According to Fig. 9.15, the decrease of the mortar thickness from 10 mm to 4 mm for masonries with rigid bricks almost double the masonry effective moduli.

On the other hand, it can be seen in Figs. 9.16 and 9.17 that \tilde{E}_{xx} and \tilde{E}_{yy} are almost nonsensitive to the change of the brick height and width. However, note that the increase of brick height a (width b) causes the increase of the effective moduli \tilde{E}_{yy} (\tilde{E}_{xx}) and $\tilde{\mu}_{xy}$. Also note that the shear effective moduli $\tilde{\mu}_{xy}$ is more sensitive to the brick’s height a than to the brick’s width b . Similar trends are observed for time evolutions of masonry’s effective tangent moduli with elastic bricks and long-term mortar’s properties (see Figs. 9.18 and 9.19 in Appendix B; Rekik et al., 2016). Quantitatively, the decrease of the mortar’s thickness only slightly affects the masonry’s effective tangent properties with elastic bricks in contrast to the rigid ones. Table 9.8 summarizes the trends of evolutions of the micro-cracked masonry’s effective moduli with variation of the parameters mortar thickness, brick height, or width.

These results allow us to conclude that effective FE predictions are as a whole more sensitive to the change of brick height “ a ” and also to the decrease of mortar thickness “ th ” for both elastic and rigid bricks. Indeed, the lowest value of brick height gives the lowest masonry stiffness. It is then more beneficial to dispose of the highest possible value for “ a .” Moreover,

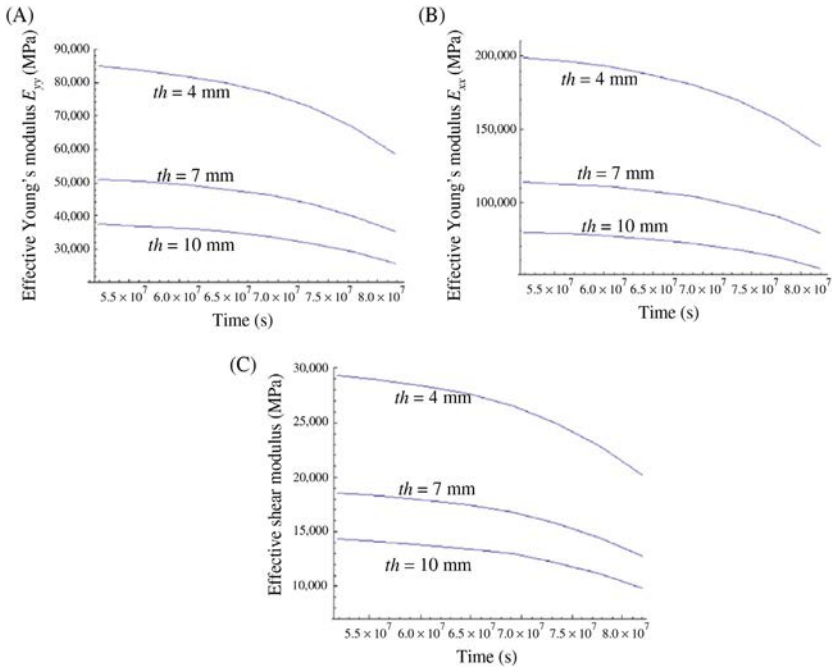


FIGURE 9.15 Masonry with rigid bricks ($E_b = 1000 E_m$ ($t = 0$)) and mortar's parameters identified at the long term: sensitivity of the FE predictions for Young's \tilde{E}_{yy} (A), \tilde{E}_{xx} ; (B) shear $\tilde{\mu}_{xy}$; and (C) moduli to mortar joint's thickness.

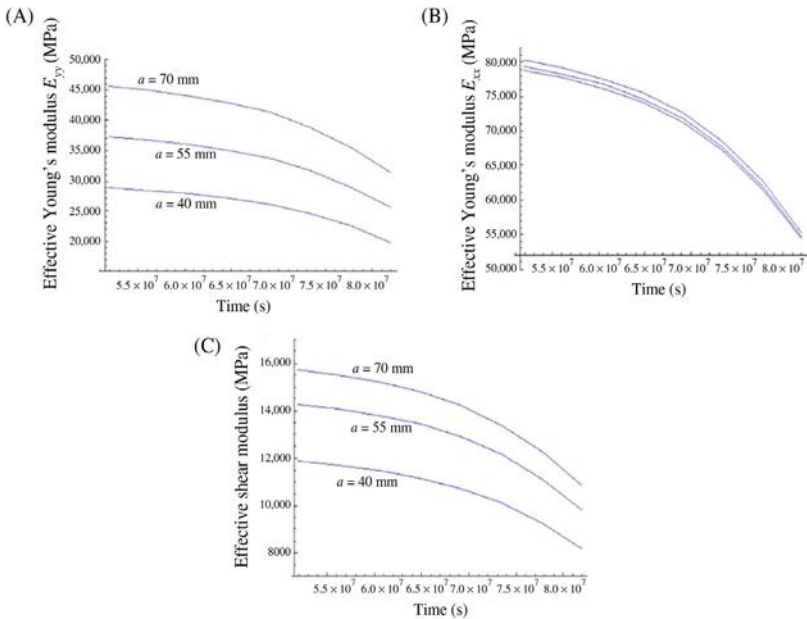


FIGURE 9.16 Masonry with mortar's parameters identified at the long term and rigid bricks ($E_b = 1000 E_m$ ($t = 0$)): sensitivity of FE predictions for Young's \tilde{E}_{yy} (A), \tilde{E}_{xx} (B); shear $\tilde{\mu}_{xy}$; and (C) moduli to the brick's height a (mm).

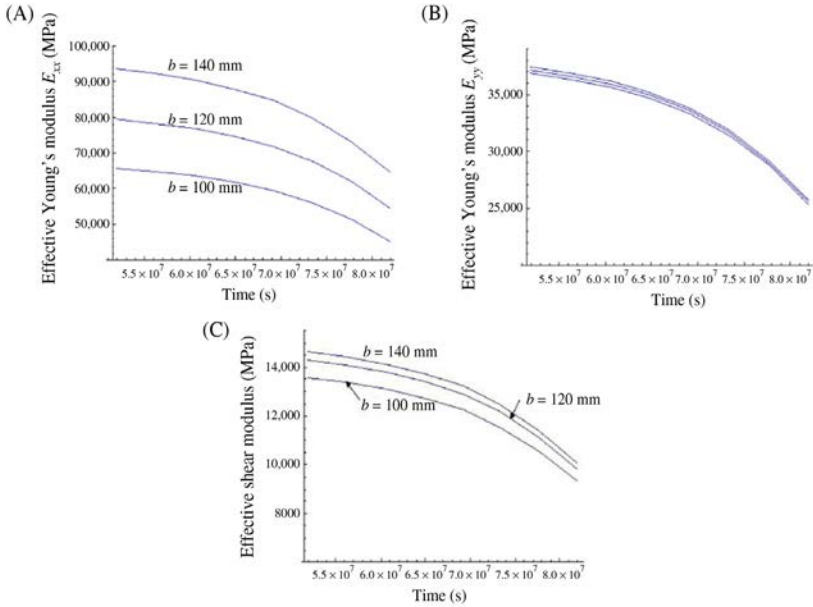


FIGURE 9.17 Masonry with mortar's parameters identified at the long term and rigid bricks ($E_b = 1000E_m$ ($t = 0$)): sensitivity of the FE predictions for Young's \tilde{E}_{yy} (A), \tilde{E}_{xx} ; (B) shear $\tilde{\mu}_{xy}$; and (C) moduli to the brick's width "b" (mm).

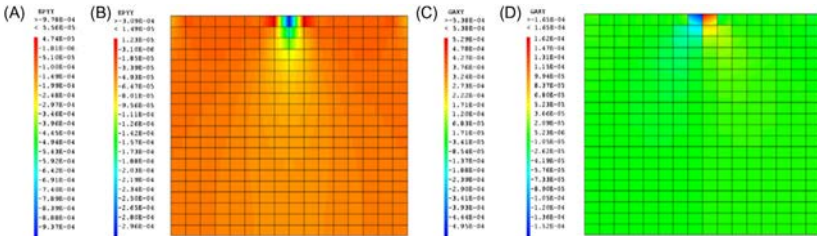


FIGURE 9.18 Comparisons at time $t = 900$ days of CTR (A and C) and FE (B and D) predictions for strain snapshots (ϵ_{yy} (A and B), ϵ_{xy} (C and D)) in the compressed wall with rigid bricks $E_b = 1000E_m$ ($t = 0$) and mortar's properties identified at the long term.

the lowest value of the mortar thickness provides the stiffest masonry mainly in the case of rigid bricks. Lastly, there is no great profit in increasing the brick width "b," which induces little increase of \tilde{E}_{yy} and $\tilde{\mu}_{xy}$ moduli.

Case of a compressed masonry panel

In this subsection, it is proposed to investigate FE predictions allowing the assessment of the relevance of the CTR model (Rekik et al., 2016) at the

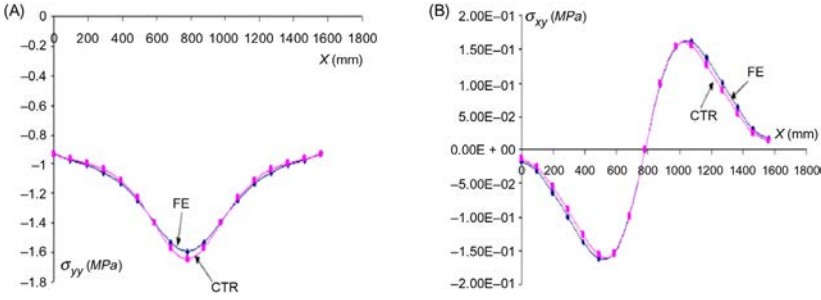


FIGURE 9.19 Comparisons at time $t = 900$ days of evolutions with abscise x of CTR and FE predictions for stress components (σ_{yy} (A) and σ_{xy} (B)) at the middle height's of the compressed wall with rigid bricks $E_b = 1000 E_m (t = 0)$ and mortar's properties identified at the long term.

TABLE 9.8 Sensitivity to various parameters (mortar thickness th , brick dimensions) of time evolutions of FE predictions for masonry effective tangent moduli with microcracked mortar and viscous parameters identified at the long term (Table 9.6).

Parameter	Bricks	E_{xx}	$\sim E_{yy}$	$\sim \mu_{xy}$
Mortar's thickness	Rigid	\uparrow for $th \downarrow$	\uparrow for $th \downarrow$	\uparrow for $th \downarrow$
	Elastic	\uparrow for $th \downarrow$ (small effect)	\uparrow for $th \downarrow$	\uparrow for $th \downarrow$
Brick's height, a	Rigid	No effect of a	\uparrow for $a \uparrow$	\uparrow for $a \uparrow$
	Elastic	\uparrow for $a \uparrow$	\uparrow for $a \uparrow$	\uparrow for $a \uparrow$ (small effect)
Brick's width, b	Rigid	\uparrow for $b \uparrow$	No effect of b	Small \uparrow for $b \uparrow$
	Elastic	\uparrow for $b \uparrow$	\sim no effect of b	Small \uparrow for $b \uparrow$

local level. For this purpose, we study the case of a masonry panel of dimensions $L = 1560$ mm (length) and $H = 1040$ mm (height) treated in Cecchi and Tralli (2012) and subjected to boundary conditions BC-2 with three distributed loads at the top and two lateral edges and an additional concentrated load F applied on the top as shown in Fig. 9.20A. Here, according to the results obtained in the “Case of a periodic unit cell: comparisons at short and long terms” section and for the sake of brevity, only the case of rigid bricks is treated ($E_b = 1000E_m (t = 0)$). The mortar inside joints are assumed to be microcracked with a matrix that obeys linear viscoelastic behavior following the MM model. Microcrack is assumed to evolve with time following the nonlinear law (9.30). On the other hand, as the arrangement of the bricks is

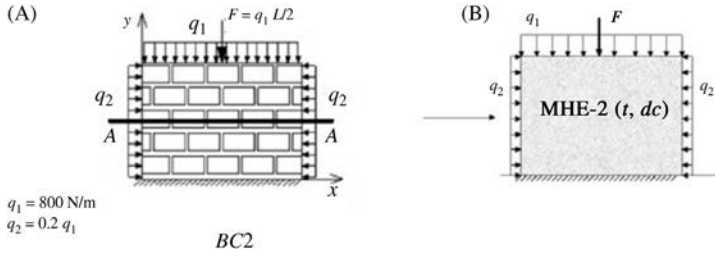


FIGURE 9.20 Equivalent problem (B) for the masonry panel submitted to boundary conditions BC-2 (A).

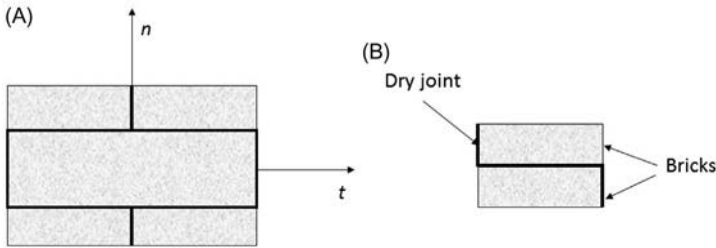


FIGURE 9.21 Periodic masonry cell (A) and its quarter part (B) considered for the modeling.

regular, the effective behavior of the panel is assumed to be well estimated by that of a periodic cell (see Fig. 9.21A). The panel can then be modeled as a homogeneous material with properties that coincide with those of the equivalent material HEM-2 (Fig. 9.20B). The mortar data used to compute this problem are those gathered at the long term as shown in Table 9.6. Qualitatively, under BC-2, distribution of the stress field σ_{yy} either for the FE or CTR model is symmetric (Fig. 9.14B) by reference to the axis of symmetry of the panel $x = L/2$ unlike that of the stress σ_{xy} which is antisymmetric (Fig. 9.14D).

Similar qualitative aspects are observed for snapshots of strains ε_{yy} (symmetric; see Fig. 9.19B) and ε_{xy} (antisymmetric according to Fig. 9.19D). Snapshots of strain (Fig. 9.18) and stress (Fig. 9.18) fields show similar localization areas at the vicinity of the application's point of the concentrated load F under condition BC-2. Quantitatively, FE and CTR estimates for stress components are close under BC-2 as shown in Fig. 9.22, illustrating evolutions of stress components along the x axis located at the middle height of the wall ($x = H/2$).

For both the FE and CTR models, as shown in the maps of the stress component σ_{yy} , except for area surrounding the application's point of load F , which is subjected to compression ($\sigma_{yy} \leq 0$), the wall is subjected locally to tensile stress ($\sigma_{yy} \geq 0$). In this area, it can be noted that the absolute values

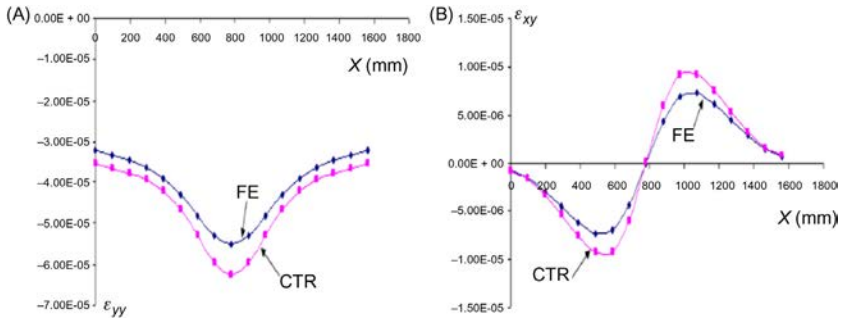


FIGURE 9.22 Comparisons at time $t = 900$ days of evolutions with abscise x of CTR and FE predictions for strain components (ε_{yy} (A) and ε_{xy} (B)) at the middle height's of the compressed wall with rigid bricks $E_b = 1000E_m$ ($t = 0$) and mortar's properties identified at the long term.

of CTR estimates for σ_{yy} and σ_{xy} are stiffer than the FE ones. Moreover, for this area, the FE and CTR estimates for shear stress σ_{xy} are close compared to local predictions for stresses σ_{yy} . In contrast, at the middle height of the wall, it can be observed that the FE and CTR estimates are close either for σ_{yy} or σ_{xy} . Moreover, CTR predictions for shear stress are slightly softer than FE ones. However, CTR estimates for σ_{yy} are slightly stiffer when $x \rightarrow L/2$; otherwise, they are almost the same. Globally, under this boundary condition, it is observed that the MM model predicts small strains. Moreover, the CTR model seems to overestimate strain localization by comparison to FE predictions. Indeed, in the area at the vicinity of the application's point of load F , local strains (ε_{yy} and ε_{xy}) derived from the CTR model are almost three to four times greater than those provided by the FE model. The evolutions of strain components ε_{yy} and ε_{xy} (Fig. 9.18) at the middle height of the wall confirm that the CTR model overestimates local strains. However, away from the area at the vicinity of the application's point of load F , the CTR and FE estimates for strain components are closer since CTR predictions are around 1.2–1.5 times greater than the FE ones.

9.2.2.6 Conclusions and perspectives

This section extends the FE homogenization method for regular microcracked viscoelastic masonries. It provides accurate orthotropic overall tangent properties for this masonry in the short and long terms. The accuracy of this model is based on similar in-plane stress hypotheses for constitutive functions in joints and bricks in contrast to the analytical model. Moreover, this accuracy is a function of both factors: numerical error function of the mesh refinement and the choice of the mean-field homogenization scheme used to assess the behavior of the microcracked mortar. Moreover, in this work, there is no recourse to the LC transform when assessing the creep behavior of the mortar. This work, which rests on the computation of the

strain localization tensors in each phase constituting the masonry (brick and mortar), proposes an alternative to an incremental homogenization approach that requires additional parameters such as the time increment and polarization tensors in viscoelastic phases. Estimates provided by the proposed numerical homogenization model serve to assess the accuracy of the recently proposed extension of the Cecchi and Taliercio's model for microcracked masonry—the CTR approach (Rekik et al., 2016)—at the local and global levels for different parameters (mortar thickness and brick dimensions). In a future work, it could be interesting to investigate the effects of more sophisticated damage evolution law functions of both time and external loading (Taliercio and Papa, 2008) on FE predictions and the accuracy of the CTR model. Moreover, the choice of the mean-field homogenization scheme could influence the overall and local results of the proposed numerical model. Indeed, a mean-field homogenization model accounting for crack interactions such as the Ponte—Castañeda and Willis model (Bornert, 2001) could be more appropriate to assess the creep behavior of microcracked mortar and to account for higher crack densities (more than 20%). At last, taking into account the creep of bricks and crack propagation as proposed in Nguyen and Dormieux (2015) for homogeneous material could improve and enrich the proposed numerical model.

9.3 Nonlinear homogenization methods for masonry

For reasons of durability and resistance to harmful factors (fire, water, chemical products, etc.), conventional bonded masonry is sometimes replaced by mortarless masonry systems such as interlocking mortarless hollow concrete block systems (Thanoon et al., 2008a); dry-stack mortarless sawn stone constructions (such as the Egyptian pyramids and the Zimbabwe ruins; Senthivel and Lourenco, 2009); and refractory linings of industrial furnaces including vessels of steel industry where the ceramic bricks are laid in direct contact with each other (Andreev et al., 2012).

In contrast to conventional mortared masonry structures, for mortarless masonry, there have been limited analytical and numerical studies, and these depend mainly on the type of blocks used to assemble the walls. Among these studies, a FE model was proposed by Oh (1994) to simulate the behavior of interlocking mortarless block developed in Drexel University. Such a procedure is useful to simulate the contact behavior of mortarless joints including geometric imperfection but is suitable only for modeling small masonry assemblies. Material nonlinearity is not considered to account for the behavior of the masonry near the ultimate load and to predict the failure mechanism. Alpa and Monetto (1998) suggested a macromodel based on homogenization techniques to model the joint and block as a homogeneous material. That model focuses on the joint movement mechanism assuming a perfect joint. This model ignores significant issues such as material

nonlinearity, joint imperfection, and progressive material failure. Recently, Thanoon et al. (2008a,b) proposed an FE model and developed an incremental iterative program to predict the behavior and failure mechanism of the system under compression. The nonlinear progressive contact behavior of mortarless joint that takes into account the geometric imperfection of the block-bed interfaces is included based on experimental testing. The developed contact relations for dry joints within specified bounds can be used for any mortarless masonry system efficiently with less computational effort. On the other hand, Senthivel and Lourenco (2009) developed a nonlinear FE analysis based on experimental data to model deformation characteristics such as load–displacement envelope diagrams and failure modes of dry-stack masonry shear walls subjected to combined axial compression and lateral shear loading. This analysis is based on a multisurface interface model where bricks and joints are assumed elastic and inelastic, respectively. More recently, Andreev et al. (2012) investigated the compressive closure of dry joints in two classes of refractory bricks: Magnesia–Carbon and Magnesia–Chromite bricks. The general aim of the investigation was to obtain data on the compressive joint closure behavior to get better insight into the masonry stress state and the joint condition during the service cycle of the furnace. To this end, the process of joint closure was measured indirectly by compressing samples with and without joints in a wide temperature range. At room temperature, direct optical measurements were also performed. FEM computer analysis was used to interpret the measurement results.

For both conventional mortared or mortarless masonry structures, a continuum model based on micromechanical considerations is preferable. Indeed, recently, especially in the case of regular masonry, efficient and reliable models based on periodic homogenization have been created to allow nonlinear analysis of large-scale structures at low numerical cost. The present work is closely connected with the latter kind of analysis. Its relevance is based on its dependence on nonlinear homogenization methods sustaining mean-field theories classically applied to nonlinear composites. In this section, it is then proposed to assess the accuracy of predictive schemes belonging to the class of secant methods (the classical; Hutchinson, 1976; Berveiller and Zaoui, 1979) and its modified approach (Ponte Castañeda, 1991; Suquet, 1995, 2001)) to the particular case of refractory mortarless masonry.

At room temperature, the nonlinear behavior of the mortarless ceramic joint was identified experimentally based on the digital image correlation (DIC) method (Rekik et al., 2015; Allaoui et al., 2017). The behavior of the brick unit was assumed to be linear elastic. Linearization procedures defining a linear comparison composite (LCC) were then applied only for the head and bed dry joint behaviors. The linear homogenization of the LCC behavior was performed using the FE method. Therefore, the approximations on the macroscopic level are related to the sole linearization procedure.

The results of nonlinear homogenization sustaining mean-field theories are compared at global and local scales to the results of the nonlinear reference solution. Furthermore, it is proposed to improve the results of the classical secant scheme to better estimate local and global behaviors of mortarless masonry. Note that the methodology proposed in this part can be enlarged to the more general case of mortared masonry or eventually for masonry at high temperatures.

9.3.1 Experimental characterization of mortarless joint behavior

In many furnaces (e.g., converters of the steel industry) Magnesia–Carbon (MaC) bricks are laid on dry joints, without mortar. Quantitative knowledge of the compressive behavior of dry joints is an essential design parameter. As an example, consider the superposition of the stress-reducing effect of the joint. For these reasons and in order to support optimization of refractory masonry structures, only the compressibility of dry joints will be investigated. Compressive tests on a stack of two MaC bricks (without mortar) were carried out. Commercially available MaC bricks were used. Their composition is shown in Table 9.9. Because of their high resistance against chemical and mechanical wear the bricks are used in the insulating linings of steel-making vessels. The morphology of the brick is bigger grains of magnesia and graphite in the matrix of small magnesia grains. The maximal grain size is 5 mm. The bricks are resin bonded.

TABLE 9.9 Chemical composition and physical properties of MaC bricks.

Material type	MaC
Density (g/cm ³)	2.93
Open porosity (%)	10
MgO (%)	98
Cr ₂ O ₃ (%)	–
CaO (%)	1
FeO ₃ (%)	0.5
Al ₂ O ₃ (%)	–
SiO ₂ (%)	0.5
Total C (%)	14

Source: From Andreev, K., Sinnema, S., Rekik, A., Allaoui, S., Blond, E., Gasser, A., 2012. Compressive behavior of dry joints in refractory ceramic masonry. *Constr. Build. Mater.* 34, 402–408.

Tests were performed at atmospheric conditions on a mechanical frame Instron 4507 with a load cell of 200 kN (Fig. 9.23). The load accuracy was about 0.2% of the reached load. The samples were cut from bricks with dimensions of $100 \times 50 \times 50 \text{ mm}^3$ and the faces were not polished. The compression tests were performed with a constant displacement rate of 0.033 mm/min. Two-dimensional DIC (Sutton et al., 1983; Vacher et al., 1999) was used to measure the compressive behavior of the dry joint with 7D correlation software (Vacher et al., 1999). The DIC is an optical method based on gray value digital images. The plane surface of the specimen was observed by a CCD camera with a resolution of 1380×1024 pixels in our case. Then, the images on the specimen surface, one before and others after deformation, were recorded, digitized, and stored in a computer as digital images. These images were compared to detect displacements by searching a matched point from one image to another using a series of mathematical mapping and cross-correlation functions. Once the location of this point in the deformed image was found, the local strain tensor was determined from the spatial distribution of the displacement field for each image.

As it is almost impossible to find the matched point using a single pixel, an area with multiple pixel points is used to perform the matching process. This area, usually called a subset, should contain several clear features, but it is often a compromise between resolution and accuracy. As a general rule, larger subset sizes will increase the accuracy, whereas smaller subsets will increase the resolution. However, realistically, the size of a subset is determined by the quality of the image and the speckle pattern. In our case, another criterion is added for the subset size. Indeed, in order to evaluate the joint behavior, the grid must be put in place on the joint and must have only a small overlap onto the bricks. For this reason, the grid steps were optimized before using the DIC analysis on joints. The chosen subset

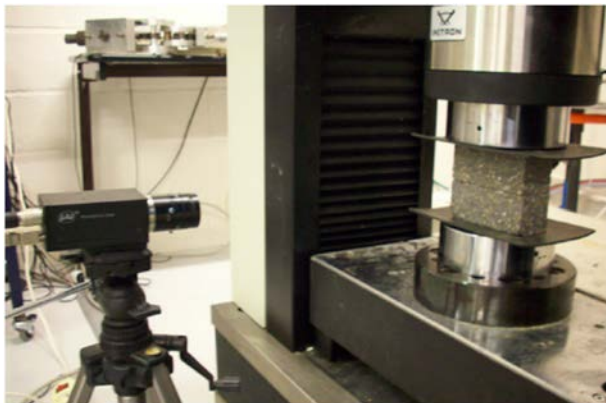


FIGURE 9.23 Experimental setup, compression test on brick-dry joint-brick laminate.

was 6×6 pixels, which corresponds to an area width of about 0.5 mm. The accuracy of the DIC reached 0.01 pixels, which represents, in our case, a resolution of 0.001 mm on the displacement. In order to perform this process, a grayscale random pattern that allows matching the subset was needed on the surface of the specimen. In our case, the natural pattern of the bricks is enough to produce a suitable pattern.

Due to roughness, shape defaults, and nonparallelism of faces, the dry joint was not horizontally aligned and its thickness was not constant. It was difficult to contain the joint in the same line of subsets. For this, measurements were performed at different locations along a joint (Fig. 9.24).

For each location, the DIC method allowed the measurement of the evolutions of the local normal ε_m , tangential ε_t , and shear ε_n strains. These strain components were averaged over each grid area and led to the dry joint compressive stress–strain curves shown in Fig. 9.25A for the third selected area, for example. Note that the DIC method does not provide the local stress in the dry joint. Moreover, as the bricks and dry joints were disposed in series, it is possible to assume that $\sigma(x)$ is set equal to the imposed normal stress $\sigma_{mn} n \otimes n$. In Fig. 9.25A, it can be seen that at the beginning, the intensive joint strain develops at relatively low stresses. With progressive loading, the reaction to the compaction increases.

At a certain stress level the joint appears to be closed completely as the closure curve aligns itself parallel to the compressive stress axis. After the joint closure, the compressive behavior of the sandwich brick/dry-joint/brick will be approximately linear. Fig. 9.25B presents an example of measurements taken at different locations of a MaC dry joint. We note that the compressive strains are different according to the place where they were determined, but the dispersion remains correct. The fluctuation of the obtained data is due to the pattern size, which is function of the microstructure size of the MaC material. The bad contact resulting from natural roughness or from the fact that the contacting surfaces were not perfectly parallel

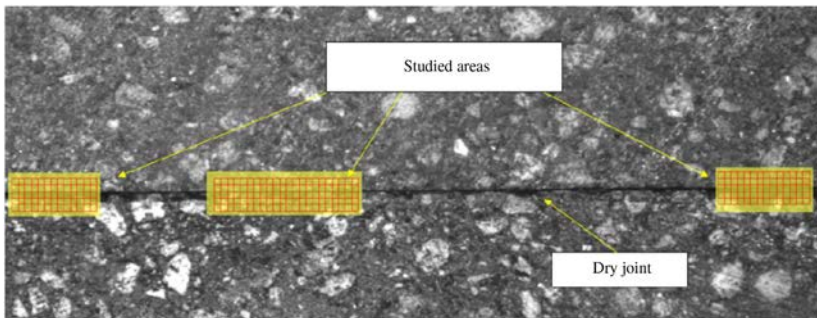


FIGURE 9.24 Optical measurement areas during a two-brick compression test (MaC).

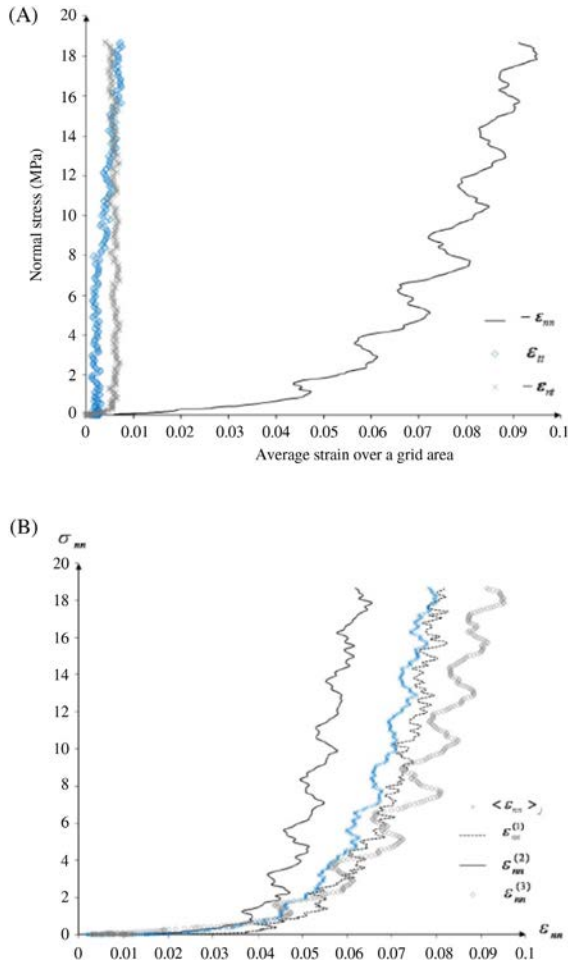


FIGURE 9.25 “Stress–strain components” curves (A) and “ $\sigma_{nn} - \epsilon_{nn}$ ” (B) evolutions at different areas selected around the mortarless joint of MaC material.

is also a parameter that influences the fluctuation and the dispersion of the measured strains.

In the following, the subscripts b and j denote the bricks and joints, respectively. The properties of the dry joint were evaluated in terms of the average over all the selected areas A_i ($i = 1, N$) of the local normal stress and strain components ϵ_{nn} , ϵ_{tt} , ϵ_{nt} , and ϵ_{zz} . Indeed, the latter component is not null under the adopted assumption of plane stress. Moreover, the shear strain components ϵ_{lz} ($l = t$ or n) are null and the strain components ϵ_{tt} and ϵ_{zz} are assumed to be equal in the (t, z) plane orthogonal to the direction of the compressive loading.

9.3.2 Nonlinear homogenization of refractory mortarless linings

Since refractory mortarless linings present periodic microstructure, it is possible to consider only a periodic cell as shown in Fig. 9.25A. Note that the MaC bricks were assumed to follow an isotropic linear elastic behavior. The behavior of the dry joints is nonlinear as identified previously by the DIC method. The lining's periodic microstructure enables a FE computation of the local and global responses. The FE result is regarded as a reference solution and denoted hereafter by NL. Note that the local and overall behavior of the mortarless masonry can also be estimated or approximated using nonlinear mean-field homogenization theories such as the classical secant procedure and its modified extension. Other “stress–strain” linearization schemes (e.g., the affine formulation) or potential-based approaches (e.g., the tangent second-order formulation) are to be addressed in the future since they need many more material parameters such as the polarization (or prestress) and the prestrain for thermoelastic “stress–strain” formulations or the potential strain energy for “potential-based” approaches.

For mortarless refractory linings, in order to assess the accuracy of the existing secant linearization schemes known to provide predictions that are too stiff for usual viscoplastic power-law composites (see, e.g., Rekik et al., 2015), it is proposed to compare their predictions at global and local scales by referencing the NL solution. Moreover, in order to evaluate the sole effect of the linearization scheme without any bias or ambiguity, it is proposed to avoid any approximation related to the linear homogenization step. The main idea relies on the adoption of an LCC with an identical microstructure to that of the original problem and to perform FE linear homogenization on this LCC using the FE method. Moreover, as the periodic cell presents two axes of symmetry—the normal and the tangential directions along the unit vectors n and t , respectively—only its quarter (see Fig. 9.25B) will be retained for computation. In this section, note that the term “exact” is set in quotation marks since the accuracy of the reference solution depends on the numerical errors and mainly on the accuracy of the adopted functions fitting the experimental data.

9.3.2.1 Reference solution: finite element nonlinear homogenization

Reference material properties of the constituents

The following power-law relation between the local normal stress σ_{nn} and normal strain ε_{nn} is identified using the experimental data for the MaC mortarless joint (see Fig. 9.26):

$$\sigma_{nn}(\varepsilon_{nn}) = E_e^j \varepsilon_{nn} + \sigma_0 \varepsilon_{nn}^{m_0} \quad (9.31)$$

where the scalars E_e^j , σ_0 (MPa) and m_0 are given in Table 9.10.

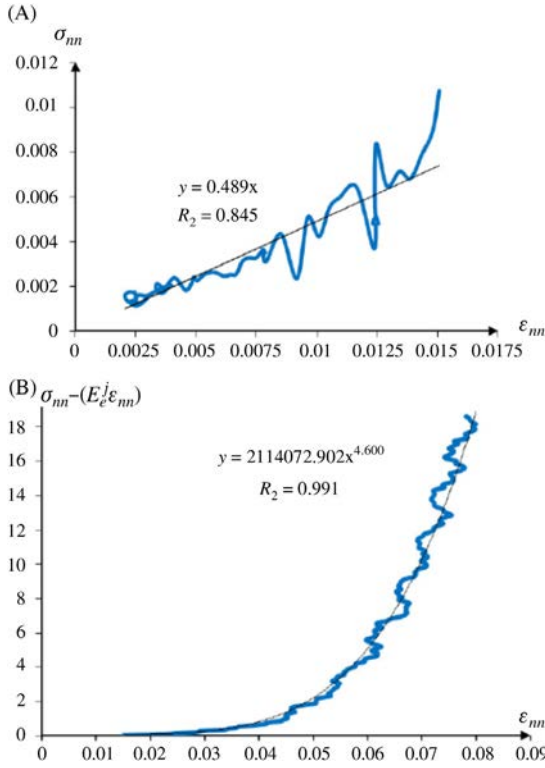


FIGURE 9.26 Evolutions of the experimental data: the linear part of the MaC mortarless joints “ $\sigma_{nn} - \varepsilon_{nn}$ ” relation (A) and “ $(\sigma_{nn} - (E_e^j \varepsilon_{nn})) - \varepsilon_{nn}$ ” evolution (B) functions of the local normal strain ε_{nn} .

Note that the scalar E_e^j can be considered as the initial Young’s modulus of the interphase since it is determined by the linear part of the curves $\sigma_{nn} - \varepsilon_{nn}$ (see Fig. 9.26A). Moreover, by analogy with the usual (concave) power-law viscoplastic materials, the constant 0 can be assumed to represent the flow stress parameter.

Note that, in the current study, the exponent m_0 is superior to 1, which is not the case for the usual viscoplastic (concave) power-law composites for which it is well known that the work-hardening exponent m is less than 1. This is due to the convex qualitative trend of the $\sigma_{nn} - \varepsilon_{nn}$ constitutive law.

The local normal compressive behavior of the dry joint can then be defined by the nonlinear convex power-law “ $\langle \sigma_{nn} \rangle_j - \langle \varepsilon_{nn} \rangle_j$ ” relationship given by Eq. (9.31). However, the transversal behavior of the considered interphase can be defined by the evolution of the ratio $-(\langle \varepsilon_{tt} \rangle^j / \langle \varepsilon_{nn} \rangle^j)$ between the tangential and normal strain field components over the interphase, denoted hereafter by the parameter ν^j , as a function of the interphase

TABLE 9.10 Parameters of the “normal stress–normal strain” relation for the MaC mortarless joint.

E_e^j	σ_0	m_0
0.489	2.11×10^6	4.6

local normal strain ε_{nn} . This evolution depicted in Fig. 9.27A can be fitted by the ensuing polynomial second-order evolution:

$$\nu^j(\varepsilon_{nn}) = c_2 \varepsilon_{nn}^2 + c_1 \varepsilon_{nn} + c_0 \quad (9.32)$$

The scalars $c_i (i = 0, 2)$ are given by Table 9.11. A linear approximation of the evolution of “ $\nu^j - \varepsilon_{nn}$ ” was avoided because it presents more than one slope (two different slopes) and the accuracy for each linear approximation is less than the 0.5 shown in Fig. 9.27A. Moreover, since this evolution (see Fig. 9.27A) is very fluctuant, a polynomial approximation of the parameter j with a degree greater than 2 was also avoided. Indeed, in practice, such polynomial approximation does not necessarily improve the accuracy shown in Fig. 9.27A—it is either inferior or not much higher (e.g., around 0.6 instead of 0.5 for a polynomial function of degree 3 or 4). For the isotropic linear elastic behavior of the MaC bricks, the Young’s modulus and Poisson’s ratio were taken, respectively, and set equal to $E_b = 10$ GPa and $\nu^b = 0.1$ (see Andreev et al., 2012).

Reference local and global behaviors of the nonlinear mortarless masonry

For the considered nonlinear problem, the local stress σ and strain ε fields in the periodic unit cell, assumed to have the volume V and to be submitted to the macroscopic strain $\bar{\varepsilon}$, are solutions of the following set of equations (Bornert, 2001):

$$\left\{ \begin{array}{l} u(x) = \bar{\varepsilon} \cdot x + u^*(x), \quad \forall x \in V \quad \text{and} \quad u^* \quad \text{on} \quad \partial V \\ \varepsilon(u(x)) = \frac{1}{2} (\nabla u(x) + {}^t \nabla u(x)) = \bar{\varepsilon} + \varepsilon(u^*(x)), \quad \forall x \in V \\ \operatorname{div}(\sigma) = 0, \quad \forall x \in V \quad \text{and} \quad \sigma \cdot n = - \quad \text{on} \quad \partial V \\ \sigma(x) = \sum_{r=j, b} \chi^r(x) g_r(\varepsilon(x)), \quad \forall x \in V \end{array} \right. \quad (9.33)$$

where u is the local displacement vector and u^* is its fluctuating part; $\chi^r(x)$ is the characteristic function of phase r (set to 1 if $x \in V^r$ and 0 otherwise); and g^r is the nonlinear constitutive law $\sigma = g^r(\varepsilon)$ followed by this phase. The general notations $- \#$ mean that the fluctuating part of the displacement vector u^* and the surface compression $\sigma \cdot n$ (n being the outer normal) are

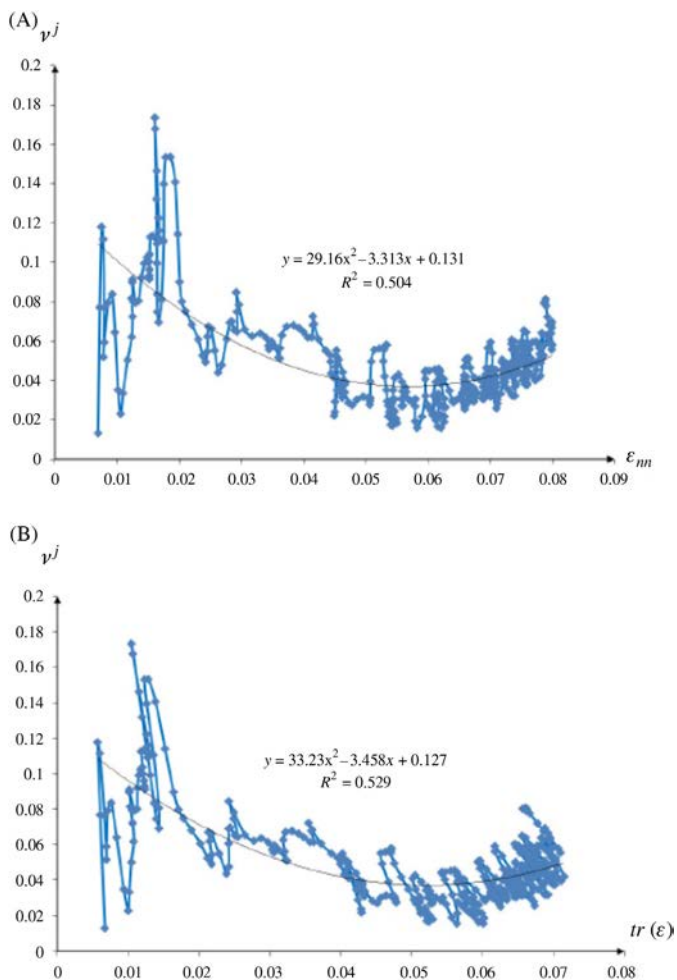


FIGURE 9.27 Evolution of the dry joint's parameter ν^j as function of (A) the local normal strain ε_{nm} and (B) the spherical part $trace(\varepsilon)$ of the local strain.

TABLE 9.11 Parameters of the evolution law of ν^j as a function of the MaC mortarless joint's local normal strain.

c_2	c_1	c_0
29.16	- 3.313	0.131

periodic and antiperiodic on the cell boundary, respectively. Note that the average $\langle \varepsilon(u^*) \rangle^j$ over the periodic unit cell of the strain field of the fluctuating part u of the displacement vector is null (Michel et al., 2001).

The local and effective behaviors of the mortarless refractory unit cell were computed using the software Cast3M (<http://www-cast3m.cea.fr/cast3m/indeIX.jsp>) under the assumption of a plane stress field. In the unit periodic cell, the joints and bricks were assumed to be perfectly bonded. To determine the effective behavior of the cell, three types of loading were applied to the periodic mortarless unit cell. Since the behavior of the dry joints can be assumed to be piecewise linear, it is possible to define at each strain increment the following macroscopic law (Eq. 9.34) where \tilde{L} denotes the instantaneous ‘‘secant’’ effective stiffness of the reference unit cell.

According to the classical Voigt notation, the constitutive behavior law of the unit cell reads:

$$\begin{pmatrix} \bar{\sigma}_{nn} \\ \bar{\sigma}_{tt} \\ \bar{\sigma}_{nt} \end{pmatrix} = \begin{pmatrix} \tilde{L}_{nnnn} & \tilde{L}_{nntt} & 0 \\ \tilde{L}_{nntt} & \tilde{L}_{tttt} & 0 \\ 0 & 0 & \tilde{L}_{ntnt} \end{pmatrix} \begin{pmatrix} \bar{\varepsilon}_{nn} \\ \bar{\varepsilon}_{tt} \\ 2\bar{\varepsilon}_{nt} \end{pmatrix} \quad (9.34)$$

where $\bar{\sigma}_{kl} = f_j \bar{\sigma}_{kl}^j + f_b \bar{\sigma}_{kl}^b$, f_r is the volume fraction of the phase r defined by $f_j = V^r/V$ and $\bar{a}^r = \langle a \rangle^r$ is the average over phase r of the stress or strain field component a .

Note that the software Cast3M provides the reference local strain and stress fields inside each phase (bricks and mortarless joints). Moreover, it allows the calculation of the average fields over each phase. For computation purposes, note that the components ε_{tt} and ε_{zz} inside the dry joint are not assumed to be equal, as is the case in the previous section, but they are given due to the FE method. The relations between the components of the effective stiffness \tilde{L}_{ijkl} and the overall elastic engineering constants (normal \tilde{E}_n and tangential \tilde{E}_t Young’s modulus, Poisson’s ratios ν_{nt} and ν_m , and shear modulus $\tilde{\mu}_m$) under plane stress assumption read:

$$\left\{ \begin{array}{l} \tilde{L}_{nnnn} = \frac{\tilde{E}_n}{1 - \tilde{\nu}_{nt}\tilde{\nu}_{tn}} \\ \tilde{L}_{tttt} = \frac{\tilde{E}_t}{1 - \tilde{\nu}_{nt}\tilde{\nu}_{tn}} \\ \tilde{L}_{nntt} = \frac{\tilde{E}_n\tilde{\nu}_{tn}}{1 - \tilde{\nu}_{nt}\tilde{\nu}_{tn}} \\ \tilde{L}_{ntnt} = \tilde{G}_m \\ \frac{\tilde{\nu}_{nt}}{\tilde{E}_n} = \frac{\tilde{\nu}_{tn}}{\tilde{E}_t} \end{array} \right. \quad (9.35)$$

To assess the effective elastic engineering constants, it is proposed to subject the unit cell to three types of loading: compression along t , compression along n , and shear loading. In the following, as we have only experimental data related to the compressive behavior of the MaC mortarless joint, we will consider only two types of loading (axial compression along n , axial compression along t). The case of shear loading is left for future work.

9.3.2.2 *Secant linearization schemes for assessing global behavior of masonry*

It is worth noting that a nonlinear mean-field homogenization approach relies on two steps: linearization and linear homogenization. The first step consists of applying one of the numerous available linearization schemes in order to linearize the nonlinear behavior and thus to define a LCC. For secant linearization schemes, the original nonlinear problem (9.36) can then be rewritten as:

$$\left\{ \begin{array}{l} u(x) = \bar{\varepsilon} \cdot x + u^*(x), \quad \forall x \in V \text{ and } u^* \# \text{ on } \partial V \\ \varepsilon(u(x)) = \frac{1}{2}(\nabla u(x) + {}^t\nabla u(x)) = \bar{\varepsilon} + \varepsilon(u^*(x)), \quad \forall x \in \\ \left. \begin{array}{l} \text{div}(\sigma) = 0, \quad \forall x \in V \text{ and } \sigma \cdot n - \# \text{ on } \partial V \\ \sigma(x) = \sum_{r=j, b} \chi^r(x) L^r(\varepsilon(x)) \\ L^r = L^r(\varepsilon^r) \end{array} \right\} \text{local linear problem} \\ \left. \begin{array}{l} \varepsilon^r = \langle \varepsilon \rangle^r \text{ (for SEC)} \text{ or } \bar{\varepsilon}^r \text{ (for VAR)} \end{array} \right\} \text{nonlinear relations} \end{array} \right\} \quad (9.36)$$

where $L^r(\varepsilon)$ are known functions whose exact expressions depend on the chosen linearization scheme. The procedure followed to solve this system of equations is described below (see “The linearization step” section). The second step of a nonlinear mean-field homogenization evaluates the effective properties of the LCC defining thus the homogeneous equivalent material (HEM). The effective properties of the HEM were assessed by applying one of the available approximative linear homogenization schemes such as the Hashin–Shtrikman (HS) bounds or the SC model (Bornert, 2001). Frequently, since such approaches induce differences between the microstructure of the nonlinear composite and that of the LCC, it is proposed in this chapter—as in Rekik et al. (2007)—to carry out an “exact” linear homogenization step by considering an LCC with an identical microstructure to that of the nonlinear composite—that is, the periodic unit cell—and using the FE method to compute the effective properties of the LCC. Accordingly, the sole effect of the linearization

step can be evaluated without any bias related to a change of microstructure or other hypothesis adopted by a classical linear homogenization scheme.

For the linearization step, it is possible to adopt one of the several linearization schemes available in the literature. Nevertheless, since the experimental data in our disposal, related to the dry joint's properties are limited, only secant linearization schemes that means the classical secant model (Hutchinson, 1976; Berveiller and Zaoui, 1979), referred to as by SEC and the modified secant method (Ponte Castañeda, 1991; Suquet, 1995, 2001) noted in the following by VAR will be treated in this chapter. The VAR method accounts for both the inter- and intraphase strain fluctuations unlike its original version, SEC, which considers only the interphase fluctuations. In the following, we propose also to test an empirical version of the classical secant method referred to as SEC_α.

The linearization step

Interphase properties in the LCC: Since a secant linearization scheme attributes to each phase r in the LCC a secant shear moduli $\tilde{\mu}_{sct}^r$ defined by the equation (Suquet, 1995; Bornert and Suquet, 2001)

$$\mu_{sct}^r(\varepsilon_{eq}) = \frac{\sigma_{eq}(\varepsilon_{eq})}{3\varepsilon_{eq}} \quad (9.37)$$

where the von Mises stress (respectively strain) measures the deviatoric part of the stress (respectively strain) tensor as done in Ponte Castañeda (1991), Gilormini et al. (2001), and Rekik et al. (2007), it is useful to define the interphase behavior in terms of the “ $\sigma_{eq} - \varepsilon_{eq}$ ” evolution as shown in Fig. 9.28 provided by the experimental data. According to the definition (9.37), the secant shear modulus of the interphase in the LCC defined by a secant linearization scheme reads:

$$\mu^j(\varepsilon_{eq}) = \mu_e^j + \mu_1 \varepsilon_{eq}^{m_1} \quad (9.38)$$

where the scalars μ_j^e and μ_1 (MPa) and the exponent m_1 are given in Table 9.12.

Note that, in this study, there is no use of the von Mises plasticity criterion since the deviatoric part of the dry joint's behavior is assumed to be nonlinear elastic following a power-law type relation. The constant μ_j^e can be considered as the elastic shear modulus of the dry joint since it is provided by the linear part (see Fig. 9.28A) of the “ $\sigma_{eq} - \varepsilon_{eq}$ ” evolution (i.e., $\mu_j^e = \sigma_{eq}(\varepsilon_{eq})/3\varepsilon_{eq}$ for $\varepsilon_{eq} \leq 0.012$). It is worth noting that a polynomial approximation of the shear modulus evolution was avoided as it could lead to aberrant (negative) values for j for some ranges of the local equivalent strain. An exponential approximation was also avoided since such function overestimates μ^j with the increase of the local equivalent strain. For this step, we chose to not linearize the spherical part of the joint's behavior but

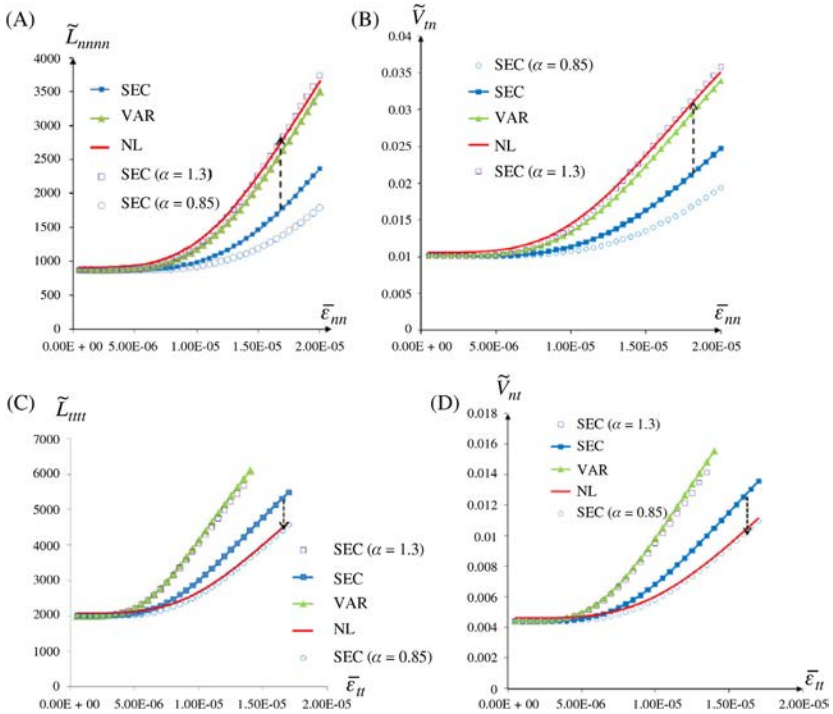


FIGURE 9.28 Periodic mortarless masonry cell under compression along n (A and B) or compression along t (C and D): effective mechanical properties versus the macroscopic strain.

TABLE 9.12 Parameters of the evolution of the dry joint's secant shear modulus versus the local equivalent strain.

μ_e^j	μ_1	m_1
0.208	10^7	4.05

to use the “exact” expression of the parameter j as a function of the spherical part $trace(\varepsilon)$ of the strain field in the joint. It reads:

$$\nu^j(tr(\varepsilon)) = b_2(tr(\varepsilon))^2 + b_1(tr(\varepsilon)) + b_0 \quad (9.39)$$

where the scalars $b_i (i = 1, 3)$ are provided in Table 9.13 and $tr(\varepsilon) = \varepsilon : i$.

The secant Young's modulus of the interphase can then be deduced as follows: $E_{sec}^j = 2^j(1 + \nu^j)$. Its bulk modulus reads $k^j = E^j/3(1 - \nu^j)$. In the LCC, the MaC interphase is then assumed to be an isotropic linear elastic phase characterized by the secant Young's modulus E_{sec}^j and the “exact”

TABLE 9.13 Parameters used to approximate the MaC dry joint's parameter $\nu^j = -(\langle \varepsilon_{tt} \rangle^j / \langle \varepsilon_{nn} \rangle^j)$ as a function of the spherical part of the strain field in the joint.

b_2	b_1	b_0
33.23	-3.46	0.127

joint's parameter ν^j (see formulae (9.39)). Recall that the term “exact” is set in quotation marks since it is related to the accuracy of the approximative function used to fit the fluctuant evolution of the parameter ν^j as a function of the spherical part of the local strain.

For the interphase, it was also possible to linearize the (convex power-law) spherical part of the MaC joint's behavior by evaluating the joint's secant bulk modulus as $k^j = \sigma_m(\varepsilon_m)/3\varepsilon_m$ and therefore to deduce the Poisson's ratio $\nu^j = (3k_{sec}^j - 2\mu_{sec}^j)/2(3k_{sec}^j + \mu_{sec}^j)$. Nevertheless, the latter secant bulk modulus k_{sec}^j risks coming to aberrant (negative) values for the Poisson's ratio if the adopted (or chosen) function fitting the “ $\sigma_m - \varepsilon_m$ ” evolution provided by the DIC method is not so accurate.

Resolution of the nonlinear problem (Eq. 9.36): To define the LCC for each loading step, the reference strain ε^r for the SEC and VAR procedures needs to be assessed. Since there is no experiment carried out on the periodic mortarless masonry cell using the DIC method as is the case for the laminate elementary structure (see Section 9.2), we do not have experimental data allowing the deduction of the reference strains ε^j for the mortarless linings. Accordingly, we propose to use an iterative method (e.g., the fixed point) in order to resolve the nonlinear set Eq. (9.36). For this nonlinear system, it is recalled that $L^r(\varepsilon)$ are known functions whose exact expressions depend on the chosen linearization procedure. Moreover, to ensure numerical accuracy in these investigations, the convergence criterion adopted for the iterative fixed-point method in this work was set equal to $10^{-6}((p_1^r + p_0^r)/2)$, where p_1^r denotes the new evaluation of the reference strain ε^r and p_0^r is its initial value in each phase r . More details about this iterative method are given in Rekik et al. (2007).

Results and discussion

This section provides insight into the influence of the secant linearization procedures on the global and local behavior of MaC regular mortarless masonry. With this aim, we consider a periodic cell made of bricks of dimensions $100 \times 50 \text{ mm}^2$ and mortarless joint with 0.104 mm thickness. This cell is discretized through a mesh relying into 50×25 , 4×50 , and 2×25 four nodes quadrilateral finite elements inside the brick, the bed, and the head joints in the quarter cell, respectively. The choice of such discretization instead of a

more refined mesh with eight-node quadrilateral finite elements was motivated by the fact that the former allows the fixed point to converge faster and due to negligible differences between results provided by both meshes. For the simulated results, it is noted that the computations are run until $\bar{\varepsilon}_m = 2 \times 10^{-5}$ ($\bar{\varepsilon}_n = 1.75 \times 10^{-5}$) for unit cells under compression along n (along t).

Effective properties Evolutions of the computed effective stiffnesses (\tilde{L}_{nnnn} , \tilde{L}_{tttt} (MPa)) and Poisson's ratios (ν_{nt} and ν_{tm}) with respect to the imposed macroscopic strain are depicted in Fig. 9.21.

For the mortarless periodic cell submitted to compression along n , the secant estimates (see Fig. 9.21A and B) reproduce qualitatively well the evolutions of the reference solutions. Moreover the VAR method provides good estimates for the effective stiffness \tilde{L}_{nnnn} and Poisson's ratio ν_{tm} of the MaC mortarless masonry. Unlike for usual viscoplastic (concave) power-law composites, the classical secant model leads to too soft overall estimates for the mortarless masonry. The SEC_{α_n} empirical model where the scalar n is found to be set to 1.3 improves the overall estimates of the classical secant procedure. Note that α_n is superior to 1. This amplification of the reference strain $\bar{\varepsilon}_{eq}^j$ for the classical secant model allows then the definition of an improved LCC more relevant than that defined by the SEC scheme.

Note that the reference strain $\alpha_n \bar{\varepsilon}_{eq}^r$ almost coincides with the second-order moment of the strain field $\bar{\bar{\varepsilon}}_{eq}^r$ (see Fig. 9.10 in Rekik et al., 2016). This argues the quasiequality between the overall predictions of SEC_{α_n} and VAR. Note that, even though the VAR model is a sophisticated model accounting for both the inter- and intraphase strain field fluctuations, the empirical model SEC_{α_n} accounting only for the interphase field fluctuations could be a satisfactory alternative for the VAR scheme as it is easier to implement and requires less theoretical investigation and numerical expense. However, it requires the implementation of an automatized inverse identification procedure not yet done in this work.

For computations carried out under compression along t (Fig. 9.21C and D), it is observed that the secant (SEC and VAR) schemes (highly) overestimate the overall reference response. The SEC_{α_t} estimates, with a scalar $\alpha_t = 0.85$ less than 1, softens the SEC estimates. Indeed, as shown in Fig. 9.10B in Rekik et al. (2016), the reference $\alpha_t \bar{\varepsilon}_{eq}^r$ is softer than the second moment $\bar{\bar{\varepsilon}}_{eq}^r$ and obviously softer than the first moment $\bar{\varepsilon}_{eq}^r$ with $\alpha_n \bar{\varepsilon}_{eq}^r \leq \bar{\varepsilon}_{eq}^r \leq \bar{\bar{\varepsilon}}_{eq}^r$. Accordingly and due to the convex qualitative trend of the " $\sigma_{eq} - \varepsilon_{eq}$ " curve for the mortarless MaC joint, the scheme SEC_{α_t} leads to better global estimate than those provided by VAR and SEC. The inequality $\bar{\varepsilon}_{eq}^r \leq \bar{\bar{\varepsilon}}_{eq}^r$ justifies also that VAR overall estimate is stiffer than that provided by SEC in the current study unlike for results obtained for usual viscoplastic (concave) power-law composites.

The different general trends observed for the SEC and VAR predictions at the global scale for mortarless masonry under compression along n and

that along t can be justified by the hypotheses adopted in this study. Indeed, for compression along t , the dry joint was assumed to behave as a joint submitted to compression along n . Moreover, the strain field components ε_{tt} and ε_{zz} were assumed to be equal, which is not necessarily true. The third hypothesis was related to the plane stress assumption for the nonlinear problem and the linear problems associated with the LCC defined by the secant schemes. Accordingly the overall trends observed for a mortarless unit under compression along n should be more rigorous. Those obtained for the mortarless unit cell under compression along t to be checked or confirmed by the investigation of the real dry joint's behavior under compression along t using DIC or another appropriate experimental technique. This idea is left for future work.

9.3.3 Conclusions and perspectives

In this section, the dry joint was assumed to be an interphase perfectly bonded with MaC bricks. Accordingly it was possible to apply mean-field homogenization theories to the mortarless masonry. A convex power-law behavior was identified for the dry joint using the DIC method for an elementary mortarless specimen under compression orthogonal to the plane of the joint. A rigorous assessment of the existing secant linearization schemes for a mortarless periodic masonry with reference to the FE solution demonstrated the superiority of the VAR model compared to the SEC scheme for mortarless unit cells under normal compression. This result confirms again—as is the case for the usual viscoplastic (concave) power-law materials—the relevance of the VAR model since it accounts for both the inter- and intraphase strain fluctuations instead of the SEC model, which considers only the interphase fluctuations. Unusually, the SEC estimates are softer than the VAR and nonlinear responses. This is due to the convex qualitative trend of the deviatoric part of the dry joint behavior instead of the usual concave trend of viscoplastic power-law composites. For mortarless unit cells under tangential compression, different trends were observed. The secant estimates, especially the VAR predictions, were found to be too stiff. To improve these results, an empirical variant SEC_α of the SEC scheme was proposed. It relies on the adjustment of a scalar in order to reduce (amplify) the reference strain $\bar{\varepsilon}_{eq}^r$ if the SEC overall estimate is stiffer (softer) than the nonlinear solution. The appropriate value of the parameter led to global and local estimates in well agreement with the reference solution. Even though the proposed model is not based on theoretical investigations and accounts only for interphase field fluctuations, it could be a satisfactory alternative for the secant schemes (SEC and VAR) if these models lead to too stiff or soft estimates.

The evaluations and comparisons carried out in the current study can be extended to mortarless refractory linings submitted to loading–unloading compressive cycles at room and high temperatures. They can also be carried

out under other mechanical tests (shear or biaxial loading) at various ranges of temperatures. However, it is important to have reliable reference solutions provided, for instance, by experiments based on the DIC method. These perspectives are left for future work. The empirical parametrical model proposed in this section for the classical secant scheme can also be applied for the VAR model. But these parametrical models require a reference solution provided by experiments or FE or FFT method. A computational inverse procedure could facilitate the determination of the tuning parameter. This approach can also be extended either for other types of brick materials or more generally for conventional mortared masonry at room or high temperatures.

References

- Alpa, G., Monetto, I., 1994. Microstructural model for dry block masonry walls with in-plane loading. *J. Mech. Phys. Solids* 42 (7), 1159–1175.
- Alpa, G., Monetto, I., 1998. Dry block assembly continuum modeling for the in-plane analysis of shear walls. In: *Proceeding of the Fourth International Symposium on Computer Methods in Structural Masonry, Italy*, pp. 111–118.
- Andreev, K., Sinnema, S., Rekik, A., Allaoui, S., Blond, E., Gasser, A., 2012. Compressive behavior of dry joints in refractory ceramic masonry. *Constr. Build. Mater.* 34, 402–408.
- Anthoine, A., 1995. Derivation of in-plane elastic characteristics of masonry through homogenization theory. *Int. J. Solids Struct.* 32 (2), 137–163.
- Berveiller, M., Zaoui, A., 1979. An extension of the self-consistent scheme to plastically-flowing polycrystals. *J. Mech. Phys. Solids* 26, 325–344.
- Beurthey, S., Zaoui, A., 2000. Structural morphology and relaxation spectra of viscoelastic heterogeneous materials. *Eur. J. Mech. A/Solids* 19, 1–16.
- Binda, L., Gatti, G., Mangano, G., Poggi, C., Sacchi-Landriani, G., 1992. The collapse of civic tower of pavia. *Masonry Int.* 6 (1), 11–20.
- Bornert, M., 2001. Homogénéisation des milieux aléatoires. In: Bornert, M., Bretheau, T., Gilormini, P. (Eds.), *Homogénéisation en Mécanique des Matériaux IX*. Tome 1, Hermes Science, pp. 133–221. Chapter 5.
- Bornert, M., Suquet, P., 2001. Propriétés non linéaires des composites: approches par les potentiels. In: Bornert, M., Bretheau, T., Gilormini, P. (Eds.), *Homogénéisation en Mécanique des Matériaux IX*. Tome 2, Hermes Science, pp. 45–90. Chapter 2.
- Brooks, J.J., 1990. Composite modeling of masonry deformation. *Mater. Struct.* 23, 241–251.
- Budiansky, B., O’Connell, R.J., 1976. Elastic moduli of cracked solid. *Int. J. Solids Struct.* 12, 81–97.
- de Buhan, P., de Felice, G., 1997. A homogenisation approach to the ultimate strength of brick masonry. *J. Mech. Phys. Solids* 45 (7), 1085–1104.
- Cecchi, A., Tralli, A., 2012. A homogenized viscoelastic model for masonry structures. *Int. J. Solids Struct.* 49, 1485–1496.
- Cecchi, A., Taliercio, A., 2013. A comparison between numerical and analytical homogenized models for visco-elastic brickwork. *XXI Congresso AIMETA Associazione Italiana di Meccanica Teorica e Applicata*. Torino, Italy, pp. 1–10.
- Chaimoon, K., Attard, M.M., 2009. Experimental and numerical investigation of masonry under three-point bending (in-plane). *Eng. Struct.* 31, 103–112.

- Chan, K.S., Bodner, S.R., Fossum, A.F., Munson, D.E., 1992. A constitutive model for inelastic flow and damage evolution in solids under triaxial compression. *Mech. Mater.* 14, 1–14.
- Chazal, C., Moutu Pitti, R., 2009. A new incremental formulation for linear viscoelastic analysis: creep differential approach. *J. Theor. Appl. Mech.* 47 (2), 397–409.
- Chengqing, W., Hong, H., 2006. Derivation of 3D masonry properties using numerical homogenization technique. *Int. J. Numer. Methods Eng.* 66, 1717–1737.
- Choi, K.K., Lissel, S.L., Taha, M.M.R., 2007. Rheological modeling of masonry creep. *Can. J. Civil Eng.* 34, 1506–1517.
- De Botton, G., Tevet-Deree, L., 2004. The response of a fiber-reinforced composite with a viscoelastic matrix phase. *J. Compos. Mater.* 38, 1255–1277.
- Deudé, V., Dormieux, L., Kondo, D., Pensée, V., 2002. Propriétés élastiques non linéaires d'un milieu mésosfissuré. *Comptes Rendus Mécanique* 330 (8), 587–592.
- Di Pasquale, S., 1992. New trends in the analysis of masonry structures. *Meccanica* 27, 173–184.
- Dormieux, L., Kondo, D., Ulm, F.J., 2006. *MicroporoMechanics*. John Wiley & Sons.
- Dubois, F., Chazal, C., Petit, C., 1999. A finite element analysis of creep-crack growth in viscoelastic media. *Mech. Time Depend. Mater.* 2, 269–286.
- Dubois, F., Chazal, C., Petit, C., 2002. Viscoelastic crack growth process in wood timbers: an approach by the finite element method for mode I fracture. *Int. J. Fract.* 113, 367–388.
- Fouchal, F., Lebon, F., Titeux, I., 2009. Contribution to the modeling of interfaces in masonry construction. *Constr. Build. Mater.* 23, 2428–2441.
- Gabor, A., Ferrier, E., Jacquelin, E., Hamelin, P., 2005. Analysis of the inplane shear behavior of FRP reinforced hollow brick masonry walls. *Struct. Eng. Mech.* 19, 237–260.
- Gabor, A., Bennani, A., Jacquelin, E., Lebon, F., 2006. Modelling approaches of the in-plane shear behavior of unreinforced and FRP strengthened masonry panels. *Comput. Struct.* 74, 277–288.
- Garavaglia, E., Lubelli, B.L., 2002. Two different stochastic approaches modeling the deterioration process of masonry wall over time. *Mater. Struct. RILEM* 35, 246–256.
- Garavaglia, E., Gianni, A., Molina, C., 2004. Reliability of porous materials: two stochastic approaches. *J. Mater. Civil Eng.* 16 (5), 419–426.
- Giambanco, G., Di Gati, L., 1997. A cohesive interface model for the structural mechanics of block masonry. *Mech. Res. Commun.* 24 (5), 503–512.
- Gilormini, G., Brenner, R., Castelnau, O., 2001. A similarity between the classical and modified secant extensions of the self-consistent model. *C. R. Mécanique* 329, 523–527.
- Hashin, Z., 1969. The inelastic inclusion problem. *Int. J. Eng. Sci.* 7, 11–36.
- Hutchinson, J., 1976. Bounds and self-consistent estimates for creep of polycrystalline materials. *Proc. Roy. Soc. Lond.* A348, 101–127.
- Huy Duong, B., 1978. *Mécanique de la Rupture Fragile*. Masson.
- Ignoul, S., Schueremans, L., Tack, J., Swinnen, L., Feytons, S., Binda, L., et al., 2007. Creep behavior of masonry structures – failure prediction based on a rheological model and laboratory tests. In: *Structural Analysis of Historical Constructions Conference*, New Delhi.
- Kim, K.S., Sing Lee, H., 2007. An incremental formulation for the prediction of two-dimensional fatigue crack growth with curved paths. *Int. J. Numer. Methods Eng.* 72, 697–721.
- Lemaitre, J.A., 1996. *Course on Damage Mechanics*, 2nd ed. Springer Verlag, Berlin.
- Li, J., Weng, G.J., 1994. Strain-rate sensitivity, relaxation behavior and complex moduli of a class of isotropic viscoplastic composites. *J. Eng. Mater. Technol.* 116, 495–504.
- Lotfi, H.R., Shing, P.B., 1994. Interface model applied to fracture of masonry structures. *J. Struct. Eng. ASCE* 120 (1), 63–80.

- Lourenco, P.B., 1998. Continuum model for masonry: parameter estimation and validation. *ASCE J. Struct. Eng.* 124 (6), 642–652.
- Lourenço, P.B., Rots, J., 1997. A multi-surface interface model for the analysis of masonry structures. *J. Eng. Mech. ASCE* 123 (7), 660–668.
- Luciano, R., Sacco, E., 1997. Homogenisation technique and damage model for old masonry material. *Int. J. Solids Struct.* 34 (24), 3191–3208.
- Mandel, J., 1966. *Cours de Mécanique des Milieux Continus*. Gauthiers-Villars, Paris.
- Marfia, S., Sacco, E., 2005. Numerical procedure for elasto-plastic no-tension model. *Int. J. Comput. Methods Eng. Sci. Mech.* 6, 99–187.
- Masiani, R., Trovalusci, P., 1996. Cauchy and Cosserat materials as continuum models of brick masonry. *Meccanica* 31, 421–432.
- Michel, J.-C., Moulinec, H., Suquet, P., 2001. Composites a microstructure périodique. In: Bornert, M., Bretheau, T., Gilormini, P. (Eds.), *Homogénéisation en Mécanique des MatériauIX*. Tome 1, Hermes Science, pp. 57–94. , Chapter 3.
- Nguyen, S.T., Dormieux, L., 2015. Propagation of micro-cracks in viscoelastic materials: analytical and numerical methods. *Int. J. Damage Mech.* 24 (4), 562–581.
- Nguyen, S.T., Dormieux, L., Le Pape, Y., Sanahuja, J., 2010. Crack propagation in viscoelastic structures: theoretical and numerical analyses. *Comput. Mater. Sci.* 50 (1), 83–91.
- Nguyen, S.T., Dormieux, L., Le Pape, Y., Sanahuja, J., 2011. A burger model for the effective behavior of a microcracked viscoelastic solid. *Int. J. Damage Mech.* 20 (8), 1116–1129.
- Oh, K., 1994. Development and investigation of failure mechanism of interlocking mortarless block masonry system. Philadelphia, Drexel University, Ph.D. thesis.
- Papa, E., Taliercio, A., 2005. A visco-damage model for brittle materials under mono-tonic and sustained stresses. *Int. J. Numer. Anal. Methods Geomech.* 29 (3), 287–310.
- Park, K., Paulino, G.H., Roesler, J.R., 2008. Determination of the kink point in the bilinear softening model for concrete. *Eng. Fract. Mech.* 75, 3806–3818.
- Pegon, P., Anthoine, A., 1997. Numerical strategies for solving continuum damage problems with softening: application to the homogenization of masonry. *Comput. Struct.* 64, 623–642.
- Pegon, P., Pinto, A., Gérardin, M., 2001. Numerical modeling of stone-block monumental structures. *Comput. Struct.* 79, 2165–2181.
- Pelissou, C., Lebon, F., 2009. Asymptotic modeling of quasi-brittle interfaces. *Comput. Struct.* 87, 1216–1223.
- Pichler, C., Lackner, R., 2009. Upscaling of viscoelastic properties of highly-filled composites: investigation of matrix inclusion-type morphologies with power-law viscoelastic material response. *Compos. Sci. Technol.* 69, 2410–2420.
- Ponte Castañeda, P., 1991. The effective mechanical properties of nonlinear isotropic composites. *J. Mech. Phys. Solids* 39 (1), 45–71.
- Raffa, M.L., Lebon, F., Rizzoni, R., 2016. On modeling brick/mortar interface via a St. Venant-Kirchhoff orthotropic soft interface. Part I: theory. *Int. J. Masonry Res. Innov.* 1 (2), 142–164.
- Raffa, M.L., Lebon, F., Rizzoni, R., 2017. On modeling brick/mortar interface via a St. Venant-Kirchhoff orthotropic soft interface. Part II: in silico analysis. *Int. J. Masonry Res. Innov.* 2 (4), 259–273.
- Reda Taha, M.M., Shrive, N.G., 2006. A model of damage and creep interaction in a quasi-brittle composite material under axial loading. *J. Mech.* 22 (4), 339–347.
- Rekik, A., Lebon, F., 2010. Identification of the representative crack length evolution for a multi-level interface model for quasi-brittle masonry. *Int. J. Solids Struct.* 47, 3011–3021.

- Rekik, A., Brenner, R., 2011. Optimization of the collocation inversion method for the linear viscoelastic homogenization. *Mech. Res. Commun.* 38, 305–308.
- Rekik, A., Lebon, F., 2012. Homogenization methods for interface modeling in damaged masonry. *Adv. Eng. Soft.* 46, 35–42.
- Rekik, A., Auslender, F., Bornert, M., Zaoui, A., 2007. Objective evaluation of linearization procedures in nonlinear homogenization: a methodology and some implications on the accuracy of micromechanical schemes. *Int. J. Solids Struct.* 44 (10), 3468–3496.
- Rekik, A., Allaoui, S., Gasser, A., Andreev, K., Blond, E., Sinnema, S., 2015. Experiments and nonlinear homogenization sustaining mean-field theories for mortarless masonry : The classical secant and its improved variants. *European Journal of Mechanics - A/Solids* 49, 67–81.
- Rekik, A., Nguyen, T.T.N., Gasser, A., 2016. Multi-level modeling of microcracked viscoelastic masonry. *Int. J. Solids Struct.* 81, 63–83.
- Rougier, Y., Stolz, C., Zaoui, A., 1994. Self-consistent modeling of elasticviscoplastic polycrystals. *C. R. Acad. Sci.* 318, 145–151.
- Sacco, E., 2009. A nonlinear homogenization procedure for periodic masonry. *Eur. J. Mech. A/ Solids* 28, 209–222.
- Schapery, R.A., 1962. Approximate methods of transform inversion for viscoelastic stress analysis. In: *Proceeding of the 4th U.S. National Congress of Applied Mechanics*, 2. ASME, pp. 1075–1085.
- Senthivel, R., Lourenco, P.B., 2009. Finite element modeling of deformation characteristics of historical stone masonry shear walls. *Eng. Struct.* 31, 1930–1943.
- Shrive, N.G., Reda Taha, M.M., 2008. Effects of creep on new masonry structures. In: Binda, L. (Ed.), *Learning from Failure – Long-Term Behaviour of Heavy Masonry Structures*. WIT Press, pp. 83–108.
- Shrive, N.G., Sayed-Ahmed, E.Y., Tilleman, D., 1997. Creep analysis of clay masonry assemblages. *Can. J. Civil Eng.* 24 (3), 367–397.
- Sukontasukkul, P., Nimityongskul, P., Mindess, S., 2004. Effect of loading rate on damage of concrete. *Cem. Concr. Res.* 34, 2127–2134.
- Sulem, J., Muhlhaus, H.B., 1997. A continuum model for periodic two-dimensional block structures. *Mech. Cohes. Frict. Mater.* 2, 31–46.
- Suquet, P., 1995. Overall properties of nonlinear composites: a modified secant moduli theory and its link with Ponte Castañeda’s nonlinear variational procedure. *C.R. Mécanique* 320, 563–571.
- Suquet, P., 2001. Nonlinear composites: secant methods and variational bounds. *Lemaitre Handbook of Materials Behaviour Models*. Academic Press, pp. 968–983, Section 10.3.
- Sutton, M.A., Wolters, W.J., Peters, W.H., Ranson, W.F., McNeill, S.R., 1983. Determination of displacements using an improved digital correlation method. *Image Vision Comput.* 1 (3), 133–139.
- Taliercio, A., Papa, E., 2008. Modelling of the long-term behavior of historical masonry towers. In: Binda, L. (Ed.), *Learning from Failure – Long-Term Behaviour of Heavy Masonry Structures*. WIT Press, pp. 153–173.
- Thanoon, W.A., Alwathaf, A.H., Noorzaei, J., Jaafar, M.S., Abdulkadir, M.R., 2008a. Finite element analysis of interlocking mortarless hollow block masonry prism. *Comput. Struct.* 86, 520–528.
- Thanoon, W.A., Alwathaf, A.H., Noorzaei, J., Jaafar, M.S., Abdulkadir, M.R., 2008b. Nonlinear finite element analysis of grouted and ungrouted hollow interlocking mortarless block masonry system. *Eng. Struct.* 30, 1560–1572.

- Tsukrov, I., Kachanov, M., 2000. Effective moduli of an anisotropic material with elliptical holes of arbitrary orientational distribution. *Int. J. Solids Struct.* 37, 5919–5941.
- Ushaksarei, R., Pietruszczak, S., 2002. Failure criterion for structural masonry based on critical plane approach. *J. Eng. Mech. ASCE* 128 (7), 769–778.
- Vacher, P., Dumoulin, S., Arrieux, R., 1999. Determination of the forming limit diagram from local measurement using digital image analysis. *CIRP Ann. Manuf. Technol.* 48 (1), 227–230.
- Verstrynge, E., Ignoul, S., Schueremans, L., Gemert, V.D., 2008. Modelling of damage accumulation in masonry subjected to a long-term compressive load. In: d’Ayala, D., Fodde, E. (Eds.), *Structural Analysis of Historic Construction*. CRC Press, pp. 525–532.
- Verstrynge, E., Schueremans, L., Van Gemert, D., Wevers, M., 2009. Monitoring and predicting masonry’s creep failure with the acoustic emission technique. *NDT E Int.* 42 (6), 518–523.
- Zucchini, A., Lourenço, P.B., 2004. A coupled homogenization-damage model for masonry cracking. *Comput. Struct.* 82, 917–929.

Further reading

- Andreev, K., Zinngrebe, E., Heijboer, W., 2009. Compressive behavior of ACS torpedo bricks. In: *11th Biennial Worldwide Conference on Unified International Technical Conference Refractories. UNITECR, Salvador (Brazil)*.
- Bagi, K., 1993. A quasi-static numerical model for micro-level analysis of granular assemblies. *Mech. Mater.* 16 (1–2), 101–110.
- Benveniste, Y., 1986. On the Mori-Tanaka method in cracked solids. *Mech. Res. Commun.* 13, 193–201.
- Brunin, J., Roulet, F., Rekik, A., Blond, E., Gasser, A., Mc Nally, R., et al., 2011. Latest evolution in Blast Furnace Hearth thermo-mechanical stress modeling. In: *4th International Conference on Modelling and Simulation of Metallurgical Processes in Steelmaking, Dusseldorf, Germany*.
- Cecchi, A., Barbieri, A., 2008. Homogenisation procedure to evaluate the effectiveness of masonry strengthening by CFRP repointing technique. *Appl. Theor. Mech.* 1 (3), 12–27.
- Chaboche, J.L., Kanoute, P., 2003. Sur les approximations “isotrope” et “anisotrope” de l’opérateur tangent pour les méthodes tangentés incrémentale et affine. *C. R. Mécanique* 331, 857–864.
- Cluni, F., Gusella, V., 2004. Homogenisation of non-periodic masonry structures. *Int. J. Solids Struct.* 41, 1911–1923.
- Cost, T.L., Becker, E.B., 2007. A multidata method of approximate Laplace transform inversion. *Int. J. Numer. Methods Eng.* 2, 207–219.
- Deng, H., Nemat-Nasser, S., 1992. Microcrack arrays in isotropic solids. *Mech. Mater.* 13, 15–36.
- Ferber, M.K., Weresczak, A.A., Hemrick, J.G., 2006. Compressive creep and thermo-physical performance of refractory materials. *Final Technical Report of Oak Ridge National Laboratory*.
- Gasser, A., Terny-Rebeyrotte, K., Boisse, P., 2004. Modelling of joint effects on refractory lining behavior. *J. Mater. Des. Appl.* 218, 19–28.
- Gasser, A., Spangenberg, J., Blond, E., Rekik, A., Andreev, K., 2011. Comparison of Different Designs of Bottom Linings with Dry Joints. *UNITECR’11, Kyoto, Japan*.
- Giambanco, G., Rizzo, S., Spallino, R., 2001. Numerical analysis of masonry structures via interface models. *Comput. Methods Appl. Mech. Eng.* 6494–6511.

- Hashin, Z., 1988. The differential scheme and its application to cracked materials. *J. Mech. Phys. Solids* 36, 719–734.
- Hoenig, A., 1979. Elastic moduli of a non-randomly cracked body. *Int. J. Solids Struct.* 15, 137–154.
- Jin, S., Harmuth, H., Gruber, D., 2014. Compressive creep testing of refractories at elevated loads – device, material law and evaluation techniques. *J. Eur. Ceram. Soc.* 34, 4037–4042.
- Laws, N., Dovrak, G.J., 1987. The effect of fiber breaks and aligned penny-shaped cracks on the stiffness and energy release rates in unidirectional composites. *Int. J. Solids Struct.* 23, 1269–1283.
- Levin, V.M., 1967. Thermal expansion coefficients of heterogeneous materials. *Mekh. Tverd. Tela.* 2, 83–94.
- Lourenco, P.B., 1996. Computational strategies for masonry structures. Delft University of Technology, The Netherlands, Ph.D. thesis.
- Lourenco, P.B., Rots, J., 1993. On the use of macro-models for the analysis of masonry shear walls. In: *Proceeding of the 2nd International Symposium on Computer Methods in Structural Masonry*, pp. 14–26.
- Masson, R., Bornert, M., Suquet, P., Zaoui, A., 2000. An affine formulation for the prediction of the effective properties of nonlinear composites and polycrystals. *J. Mech. Phys. Solids* 48, 1203–1227.
- Molinari, A., Toth, L.S., 1994. Tuning a self-consistent visco-plastic model by finite element results, part I: modeling. *Acta Metall. Mater.* 42, 2453–2458.
- Molinari, A., Ahzi, S., Kouddane, R., 1997. On the self-consistent modeling of elastic-plastic behavior of polycrystals. *Mech. Mater.* 26, 43–62.
- Nguyen, T.M.H., Blond, E., Gasser, A., Prietl, T., 2009. Mechanical homogenisation of masonry wall without mortar. *Eur. J. Mech. A/Solids* 28 (3), 535–544.
- Nguyen, T.T.N., Rekik, A., Gasser, A., 2014. A multi-level approach for micro-cracked masonry. In: *11th World Congress on Computational Mechanics (WCCM XI)*, Barcelona.
- Parvanova, S., Gospodiniv, G., in press. Development of “event-to-event” nonlinear technique to lightly reinforced concrete beams by simplified constitutive modeling. *Int. J. Solids Struct.*
- Ponte-Castañeda, P., Willis, J.R., 1995. The effect of spatial distribution on the behavior of composite materials and cracked media. *J. Mech. Phys. Solids* 43, 1919–1951.
- Rekik, A., 2006. Une méthodologie pour une évaluation précise des procédures de linéarisation en homogénéisation non linéaire. Ecole Polytechnique, Ph.D. thesis.